Post-event information in annual satellite embeddings inflates the apparent performance of landslide susceptibility models: a paired audit of 18 events

Yifan Du*, https://orcid.org/0009-0008-7740-5408
Tianhe Zheng, https://orcid.org/0009-0000-8993-814X
Peiyan Yang, https://orcid.org/0009-0004-6214-0831
Yibo Li, https://orcid.org/0009-0002-2926-757X
Junhang Zhou, https://orcid.org/0009-0002-0458-2127
Kun Yang, https://orcid.org/0009-0006-6609-219X

North China University of Water Resources and Electric Power, 136 Jinshui East Road, Zhengzhou 450046, Henan, China

*Corresponding author: Yifan Du, duyifan619916@gmail.com

This manuscript is a preprint and has not been peer reviewed. It has been submitted to *Landslides*. Subsequent versions may differ. Code, analysis log and derived data: https://doi.org/10.5281/zenodo.23952287. Online Resource 1 is appended.

Abstract

Landslide susceptibility models are often evaluated by spatial cross-validation on the inventory of a single event. When predictors come from annual satellite products, the layer for the event year can also record the event's aftermath. We audited 18 earthquake- and rainfall-triggered events with 61,402 landslide locations, changing only the input year of AlphaEarth Foundations embeddings while samples, spatial folds and models stayed fixed. Event-year inputs raised the area under the receiver operating characteristic curve (AUC) by 0.0874 (95% confidence interval 0.0649–0.1098) for a point model and 0.0705 (0.0475–0.0934) for a patch model. The increase persisted after correction for pre-event drift and appeared in point inventories and in inventories with mapped extents. Sentinel-2 inputs with a fixed number of dates gained discrimination when the observation window moved past the event. Across two municipalities affected by the May 2023 Emilia-Romagna event, the highest-scoring 10% of the area captured 30.0% of the mapped landslide area with prior-year inputs and 49.3% with event-year inputs. The event-year layer replaced 46.4% of that top-ranked area. These are within-event validation results, not forecasting skill. In retrospective tests trained on earlier landslides with pre-target inputs, embeddings added 0.059 AUC beyond conventional factors and landslide history in North Carolina. In Lushan they added 0.008, and the interval included zero. Susceptibility assessments that use annual satellite products should report the observation window of each predictor, the chronology of the inventory and the evaluation domain.

Keywords: Landslide susceptibility · Temporal leakage · Spatial cross-validation · Landslide inventories · Historical landslides · AlphaEarth Foundations

Introduction

Landslide susceptibility maps are meant to show where future landslides are more likely, and they support zoning for land-use planning (Fell et al. 2008; Reichenbach et al. 2018). Their quality is usually judged against mapped landslides, often from the inventory that calibrated the model (Guzzetti et al. 2006). Such a test measures how well a model separates known failures from other terrain. Whether a map anticipates later landslides is a different question, which posterior evaluation against landslides that occurred after the map was made addresses directly

(Pareek et al. 2025). A within-event test speaks to that second question only if the predictors describe the terrain as it was before the event.

Several sources of optimism in susceptibility evaluation are well documented. Spatial dependence between training and test locations inflates random cross-validation, and spatial blocking reduces this effect (Brenning 2005; Roberts et al. 2017; Ploton et al. 2020; Karasiak et al. 2022). Chrono-validation trains on earlier failures and tests on later ones (Lombardo and Tanyas 2020), and the time span of the training inventory changes the resulting assessment (Zhu et al. 2026). Where landslides are sampled within mapped polygons also changes the fitted model (Ersayin 2026). Steger et al. (2020) examined how post-failure topography in the elevation data affects data-driven susceptibility models. These studies concern the labels, their sampling and the terrain model. Machine learning is now widely used for susceptibility modelling (Merghadi et al. 2020), and image-derived predictors raise a related question: when were their observations made?

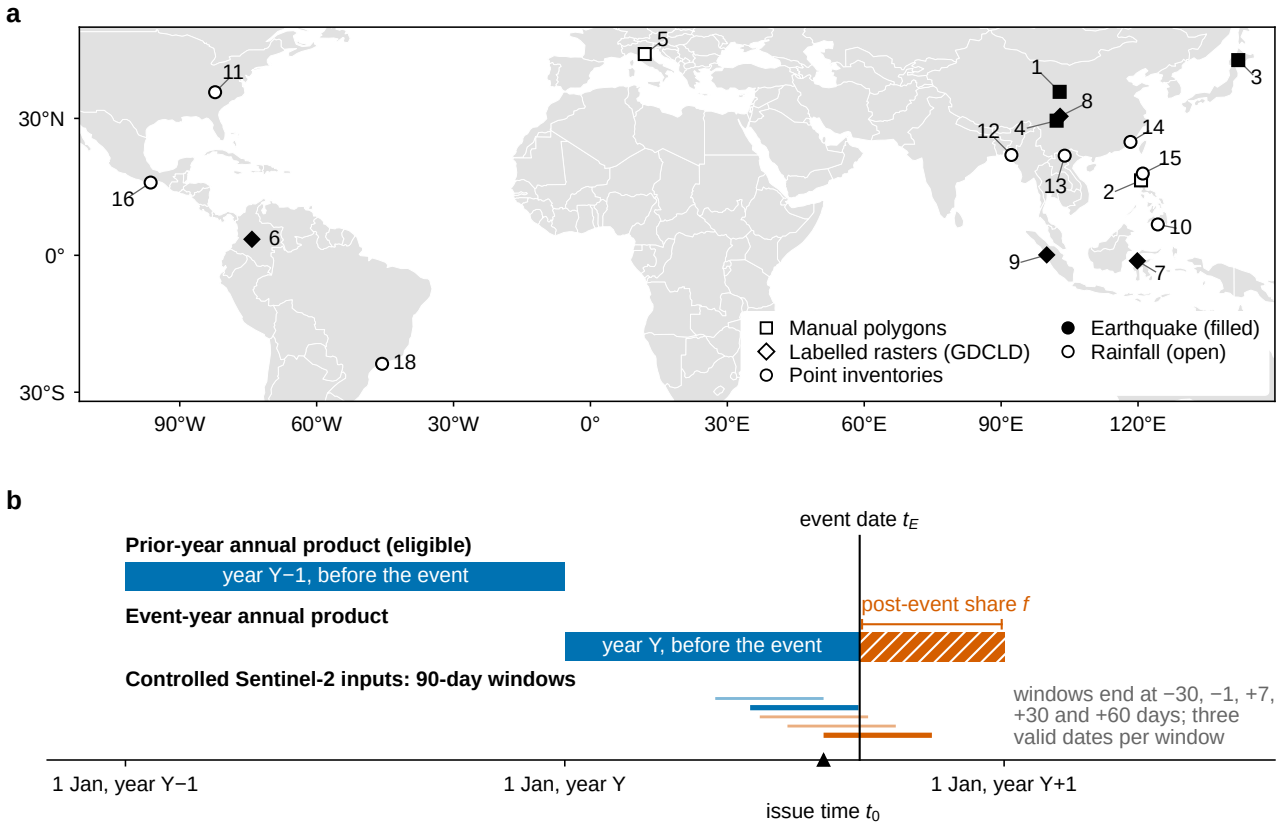
Annual satellite embeddings make that question practical. AlphaEarth Foundations (AEF) compresses multisensor observations into a 64-dimensional vector per 10 m pixel and calendar year (Brown et al. 2025). TESSERA summarizes Sentinel-1 and Sentinel-2 time series in 128 dimensions (Feng et al. 2025). Both products are free and global. They have been used for landslide mapping and susceptibility (Cheng et al. 2026; Fang et al. 2026; Li et al. 2026; Liu et al. 2026) and for other hazards (Knezevic et al. 2026; Thasma et al. 2026; Zhuang et al. 2026). An annual layer carries a year label but no visible observation dates. For an event in May, most event-year observations follow the event and can record scars, removed vegetation and deposits. Spatial blocking does not remove this information, because each test location carries its own post-event surface. This is leakage in the sense of Kaufman et al. (2012) and Kapoor and Narayanan (2023). Recent applications differ in this respect. Some used layers that include the event year, whereas Fang et al. (2026) used previous-year embeddings with temporal and spatial holdouts (Online Resource 1, Text S5).

We ask three questions with a paired audit of 18 events. First, how much does the input year change within-event evaluation, and does the change depend on the inventory type? Second, how does it change map evaluation at a fixed area budget, including which areas rank highest? Third, when models are trained on earlier landslides, how much do pre-target embeddings add beyond conventional factors and explicit landslide history? The audit changes only the input year and holds samples, spatial folds and models fixed. Controls for pre-event drift, Sentinel-2 windows with a fixed number of dates and a decomposition of the modelling workflow test where the effect comes from. Code, per-sample predictions and provenance tables are released for reuse.

Materials and methods

Temporal design

Let t0 be the time at which an assessment is issued and tE the time of the target event. An input is eligible when its observations end no later than t0 and t0 < tE. We distinguish three validation designs (Fig. 1c). A within-event audit swaps the input year while the labels of one event stay fixed. A retrospective forward test trains on earlier landslides and uses observations made before the target. Historical deployment also requires that products, encoders and confirmed training records were available at t0; we do not attempt it. AEF was released on 30 July 2025 (Google DeepMind 2025), so all AEF layers are used retrospectively.



c

Design	Training labels	Inputs	Question answered	This study
Within-event audit	Same event, spatial folds	Annual layer of year Y−1 or Y (year swapped)	How much the input year changes one evaluation	Figs. 2–5
Retrospective forward test	Earlier landslides only	Observations made before the target	What information exists before the target	Fig. 6
Historical deployment	Records confirmed by t_0	Products and encoders released by t_0	Whether a forecast could have been issued at t_0	Not attempted

Fig. 1 Study events and temporal design. **a** Event locations, numbered as in Table 1; marker shape gives the inventory form, and open markers are rainfall events. **b** A calendar-year product for the event year Y contains observations made after the event date tE (hatched share f), whereas the prior-year product ends before tE. The controlled Sentinel-2 inputs use 90-day windows that end at fixed offsets from tE. **c** Three validation designs, the information each may use and the question each can answer. Country outlines: Natural Earth (public domain)

Eligibility is defined relative to the current target. A 2021 embedding at the site of a 2013 landslide is an eligible pre-target observation for a 2022 event, because the 2013 failure is history for that target. Auxiliary layers follow the same rule. WorldCover 2021 (Zanaga et al. 2022) enters the 2022 and 2024 retrospective tests but is not pre-event information for the 2018–2019 events, and the embedding-only contrasts do not use it.

Events, inventories and samples

The collection contains seven earthquake and eleven rainfall events from 2018–2024, with 61,402 landslide locations and 117,059 controls (Table 1). Nine inventories map landslide extents: five as manual polygons and four as manually labelled GDCLD rasters (Fang et al. 2024). The other nine are point inventories: eight satellite-mapped COOLR events (Juang et al. 2019; Mancino et al. 2025) and the rapid-response inventory of Hurricane Helene (Burgi et al. 2025). None comes with a verified survey boundary that is independent of the

mapped landslides. Two auxiliary events with model-generated labels are excluded from pooling.

Mapped objects and point records represent different things. Each polygon or raster object contributes one point at its highest cell in the Copernicus GLO-30 DEM (European Space Agency 2022). This crown proxy approximates the upper part of a failure; it is not a field-verified initiation point. Point records are used as reported and deduplicated at 30 m. Controls for mapped inventories and Helene lie on slopes >5° and 100–2,000 m from mapped failures, within the label footprint, the inventory hull plus 1 km or, for Emilia-Romagna, the regional survey area. COOLR controls lie 300–3,000 m from event points, more than 200 m from any event point and on slopes >5°. These sampling domains support paired comparisons of predictors within an event; they do not make the controls verified stable ground (Online Resource 1, Text S1).

Table 1 Events and audit samples, grouped by inventory form and ordered by the post-event fraction f, the share of the calendar year after the reference date (365-day approximation). AEF layers from Y−2 to Y+2 were used where available; AEF begins in 2017, so Palu, Mangkhut and Eastern Iburi have no Y−2 layer

No.	Event (country)	Trigger, date	f	Inventory source	Control domain	Landslides / controls
	Manual polygons: one crown proxy per object					
1	Jishishan (China)	earthquake, 2023-12-18	0.04	Jin and Chen (2025)	hull + 1 km	10,740 / 21,480
2	Mangkhut, Itogon (Philippines)	rainfall, 2018-09-15[b]	0.29	Abancó et al. (2021); Abancó and Jones (2023)	hull + 1 km	1,100 / 2,200
3	Eastern Iburi (Japan)	earthquake, 2018-09-06	0.32	Zhang et al. (2019)	hull + 1 km	5,625 / 11,250
4	Luding (China)	earthquake, 2022-09-05	0.32	Liu et al. (2025)	hull + 1 km	8,385 / 16,770
5	Emilia-Romagna (Italy)	rainfall, 2023-05-16[a]	0.63	Pizziolo et al. (2024)	regional survey area	15,000 / 30,000
	Labelled rasters (GDCLD): one crown proxy per object					
6	Mesetas (Colombia)	earthquake, 2019-12-24	0.02	Fang et al. (2024)	label footprint	1,990 / 3,980
7	Palu (Indonesia)	earthquake, 2018-09-28	0.26	Fang et al. (2024)	label footprint	1,522 / 3,044
8	Lushan (China)	earthquake, 2022-06-01	0.58	Fang et al. (2024)	label footprint	1,286 / 2,572
9	Pasaman, West Sumatra (Indonesia)	earthquake, 2022-02-25	0.85	Fang et al. (2024)	label footprint	484 / 968
	Point inventories: reported point					
10	Nalgae, Mindanao (Philippines)	rainfall, 2022-10-28[c]	0.18	COOLR	0.3–3 km offsets	208 / 416
11	Helene, southern Appalachians (USA)	rainfall, 2024-09-27	0.26	Burgi et al. (2025)	hull + 1 km	2,213 / 4,426
12	Chittagong (Bangladesh)	rainfall, 2023-08-16[c]	0.38	COOLR	0.3–3 km offsets	1,764 / 2,921
13	Northern Vietnam	rainfall, 2023-08-04[c]	0.41	COOLR	0.3–3 km offsets	1,891 / 3,053
14	Fujian (China)	rainfall, 2023-07-28[c]	0.43	COOLR	0.3–3 km offsets	345 / 691
15	Luzon (Philippines)	rainfall, 2023-07-26[c]	0.43	COOLR	0.3–3 km offsets	3,133 / 6,422
16	Agatha (Mexico)	rainfall, 2022-05-30[c]	0.59	COOLR	0.3–3 km offsets	3,756 / 3,527
17	Freddy (Malawi)	rainfall, 2023-03-12[c]	0.81	COOLR	0.3–3 km offsets	1,634 / 2,948
18	São Paulo coast (Brazil)	rainfall, 2023-02-19[c]	0.86	COOLR	0.3–3 km offsets	326 / 391

[a] Two storms (2–3 and 16–17 May 2023); 16 May is the reference date. [b] Mapped on imagery from February 2018 to March 2019, so some changes precede the typhoon. [c] COOLR via UGLC (Juang et al. 2019; Mancino et al. 2025); the trigger date is catalogued, and the timing of each label was not verified independently.

Satellite inputs

AEF Satellite Embedding V1 was read from the Source Cooperative mirror. Signed 8-bit values v were dequantized as $\text{sign}(v)(v/127.5)^2$, with mask, completeness and vector-norm checks. TESSERA comparisons use identical point sets in ten events; seven have v1 coverage and three use v1.1-cam. A conventional Sentinel-2 baseline uses nine-channel annual Level-2A reflectance and index composites. Static factors are slope, aspect sine and cosine, curvature, 330 m relief and elevation. The retrospective models also use log upslope area (Bartos et al. 2024), WorldCover 2021 (Zanaga et al. 2022) and, in North Carolina, PRISM precipitation climatology (Daly et al. 2008). Online Resource 2 lists the AEF and TESSERA source files.

Paired year substitutions and workflow decomposition

Samples, controls, spatial folds, buffers and model settings are identical across input years. Spatial k-means defines five folds (ten for Emilia-Romagna), and training locations within 500 m of test locations are removed. The point model is LightGBM (Ke et al. 2017) with 400 trees, 63 leaves, learning rate 0.05 and row and feature subsampling of 0.8. The patch model is the CNN2D of Cheng et al. (2026) on 11 × 11 cells at 30 m. It is trained with three seeds, Adam (initial learning rate 0.001), batch size 512 and at most 200 epochs. Early stopping uses a stratified 15% of each buffered training fold. The two models differ in resolution and spatial context as well as in architecture (Online Resource 1, Text S1 and Table S1).

For event year Y, the event-year increment is $d0 = \text{AUC}(Y) - \text{AUC}(Y-1)$. The placebo $\text{AUC}(Y-1) - \text{AUC}(Y-2)$ measures ordinary annual drift, and subtracting it gives the excess over that drift; it is available for 15 events. The year-after increment is $d1 = \text{AUC}(Y+1) - \text{AUC}(Y-1)$.

A training-year × prediction-year comparison separates three components. Write $\text{AUC}(a \to b)$ for a model trained on year-a inputs and evaluated with year-b inputs. The prediction-only component is then $P = \text{AUC}(Y-1 \to Y) - \text{AUC}(Y-1 \to Y-1)$, the training-only component is $T = \text{AUC}(Y \to Y-1) - \text{AUC}(Y-1 \to Y-1)$, and the interaction is $I = d0 - P - T$. P corresponds to applying a pre-event model to an event-year layer, and d0 to building and testing the model on event-year layers.

Controlled Sentinel-2 windows

Two events test the role of observation time directly. At Eastern Iburi and Mangkhut, one interior point per inventory polygon (1,100 per event) and 2,200 controls were linked to all Sentinel-2 L2A scenes. Ninety-day windows end at −30, −1, +7, +30 or +60 days relative to the event. Each point and window contributes exactly three valid dates per draw, so moving the window end changes when the observations were made but not how many there are. Five features are computed after temporal truncation: median red, near-infrared and NDVI, and the 10th and 90th NDVI percentiles. Ten date-sampling seeds each produce a separate LightGBM fit and spatial out-of-fold prediction, and the ten AUCs are averaged. The preceding year provides a seasonal reference, $D = [\text{AUC}2018(+60) - \text{AUC}2018(-1)] - [\text{AUC}2017(+60) - \text{AUC}2017(-1)]$, on the points with at least three dates in all four endpoint windows. Online Resource 1 documents scene scaling, quality masks, sample flow and support selection (Text S2, Tables S6–S9 and S22).

Retrospective tests with explicit landslide history

North Carolina training records are the 2,711 USLI v3 landslides (Belair et al. 2025) with confidence ≥5 and an occurrence interval ending before 1 January 2024. Controls lie on slopes >5° and more than 100 m from these records. They are drawn at a 2:1 ratio within 5 km strata of the records' convex hull plus 1 km. Neither target locations nor date-ineligible records define this domain. The target is Helene, with 2,025 landslides and 3,685 controls. USLI v3 was published in February 2025, so this is an occurrence-bounded retrospective test.

Lushan uses 8,833 landslides of the 2013 earthquake and 17,666 controls (Xu et al. 2015) to predict the June 2022 event (1,286 landslides and 2,572 controls). Its training domain excludes the convex hull of the target sample plus 1 km, a spatial separation defined retrospectively.

Table 2 lists the schemes. History enters as log(1 + distance to the nearest earlier landslide) and log(1 + number of earlier landslides within 1 km). A training positive excludes only its own source record, so neighbouring records remain. Distances ≤100 m and >100 m define near- and far-history strata for both classes; they describe proximity, not reactivation of the same landslide. All schemes use 500 LightGBM trees, otherwise unchanged settings and seed 0, without tuning on the test set (Online Resource 1, Text S3).

Table 2 Retrospective schemes. Conventional factors comprise the available terrain, land-cover, hydrological and climatic variables; lithology and roads are not included. Historical records are qualified against the current target

Scheme	Inputs	Comparison addressed
B0	Conventional factors	Reference discrimination
H	Historical distance and count	Historical spatial signal alone
B1	B0 + historical distance and count	Added value of explicit history
B2	Prior-year AEF	Pre-target embedding value
B3	B1 + prior-year AEF	Embedding increment beyond factors and history
B0 + AEF	B0 + prior-year AEF	Fusion without explicit history
Post-event diagnostic	Fixed B2 model, event-year AEF at prediction	Response to post-target input

Map domains and area-based evaluation

Nine events with mapped extents have 30 m spatial out-of-fold maps. Their domains comprise label footprints or polygon hulls, slopes >5°, locations within 2 km of the target inventory and valid AEF inputs in all compared years. We call them target-conditioned domains, because their extent depends on where landslides occurred. A second design covers the full administrative area of Brisighella and Modigliana (about 297 km², 329,953 cells at 30 m). Its labels come from the inventory of Ferrario (2023) and Ferrario and Livio (2024), and its extent does not depend on the target landslides. Scores average five saved spatial out-of-fold designs, and every cell has predictions in all compared years. The two municipalities form one event-level test.

The map endpoint is top-area capture, the share of mapped landslide area within the highest-scoring 5%, 10% or 20% of the evaluated area; tied boundary scores share the budget proportionally. Capture counts complete landslide areas, whereas training used crown proxies, so the captured area can include transport and deposition zones. It does not show that a model predicts those processes. Capture is not precision either, because its denominator is the total mapped landslide area. ROC AUC compares mapped landslide cells with the rest of the domain, and average precision uses the same labels. Intervals come from a paired spatial-cluster bootstrap (Online Resource 1, Text S4).

To see which areas change rank, we compared the top-ranked areas of two input years in the administrative

domain. Let wa and wb be the selection weights of the two years (1 inside the budget, fractional for tied boundary cells). Overlap is the weighted Jaccard index J = Σmin(wa, wb)/Σmax(wa, wb), and the replaced share is R = 1 − Σmin(wa, wb)/Σwa. The pre-event pair 2021–2022 gives a reference for ordinary turnover between annual layers; independent random rankings would give J = 0.053 and R = 0.90 at the 10% budget. Intervals use the clusters and bootstrap weights of the capture estimates, with the selection recomputed in every replicate. The 5% and 20% budgets and the five individual spatial designs were specified as sensitivity checks before computation (Online Resource 1, Text S6).

Statistical analysis

The event, not the landslide, is the unit of pooling. Event-level means use the DerSimonian–Laird (DL) estimator (DerSimonian and Laird 1986). REML with Hartung–Knapp–Sidik–Jonkman (HKSJ) intervals is a robustness analysis and gives the between-event heterogeneity (Hartung and Knapp 2001; Viechtbauer 2005; IntHout et al. 2014). Approximate prediction intervals for a new event combine heterogeneity and the uncertainty of the mean with a t reference on k − 2 degrees of freedom. We also omit one event or one country group at a time. Equivalence tests use margins of ±0.01 for point AUC and ±0.02 for map capture (Schuirmann 1987; Lakens 2017). The principal AUC ranks pooled out-of-fold scores; a sensitivity analysis compares only positive–negative pairs within each fold (Online Resource 1, Text S4). For the inventory comparison, events were grouped into inventories with mapped extents (k = 9) and point inventories (k = 9). Group means use the DL estimator, and the group difference is also estimated by a REML meta-regression with a Knapp–Hartung interval. Bootstrap intervals condition on the fitted models and on the sampled inventory. A local analysis log records each analysis plan before its computation; it is not a public preregistration.

Results

Event-year inputs inflate within-event AUC in all inventory types

With prior-year AEF, the median within-event AUC was 0.81 for the point model and 0.80 for the patch model. Event-year inputs increased AUC in all 18 point-model events and in 16 of 18 patch-model events (Fig. 2). The mean increments were 0.0874 (95% CI 0.0649–0.1098) and 0.0705 (0.0475–0.0934). Subtracting the preceding annual drift left 0.085 (0.057–0.113) and 0.064 (0.035–0.093) across 15 events, and both placebos were equivalent to zero within the specified margins. Leaving out one event or country gave point effects of 0.080–0.094 and patch effects of 0.062–0.077. REML between-event standard deviations were 0.050 and 0.053 AUC, and the approximate prediction intervals for a new event were −0.022 to 0.197 (point) and −0.044 to 0.186 (patch). The average effect is stable, whereas single events range from negligible to large.

The increase was not confined to one inventory form (Fig. 2; Table S23). For the point model, inventories with mapped extents gave a mean of 0.064 (0.040–0.087) and point inventories 0.111 (0.077–0.145), and all nine events in each group were positive. The patch model gave 0.065 (0.037–0.093) and 0.075 (0.039–0.111). The larger point-model mean for point inventories was not robust: the meta-regression difference was 0.046 (−0.002 to 0.094). All nine point inventories are rainfall events and eight of them use offset controls, whereas seven of the nine mapped inventories are earthquakes. Inventory form therefore cannot be separated from trigger and sampling design.

Two further checks concern the metric and the preprocessing. Comparing only within-fold positive–negative pairs gave mean increments of 0.082 (0.062–0.103) and 0.069 (0.050–0.088). Point-model increments stayed

positive in 17 of 18 events; Jishishan changed from +0.026 to −0.010 (Table S19). Mangkhut had the most missing patch cells. There, estimating the imputation means only from the inner fitting subset changed the CNN increment from 0.1073 to 0.1096, a paired change of +0.0024 (+0.0003 to +0.0045) (Table S21). This check was not repeated in the other 17 events.

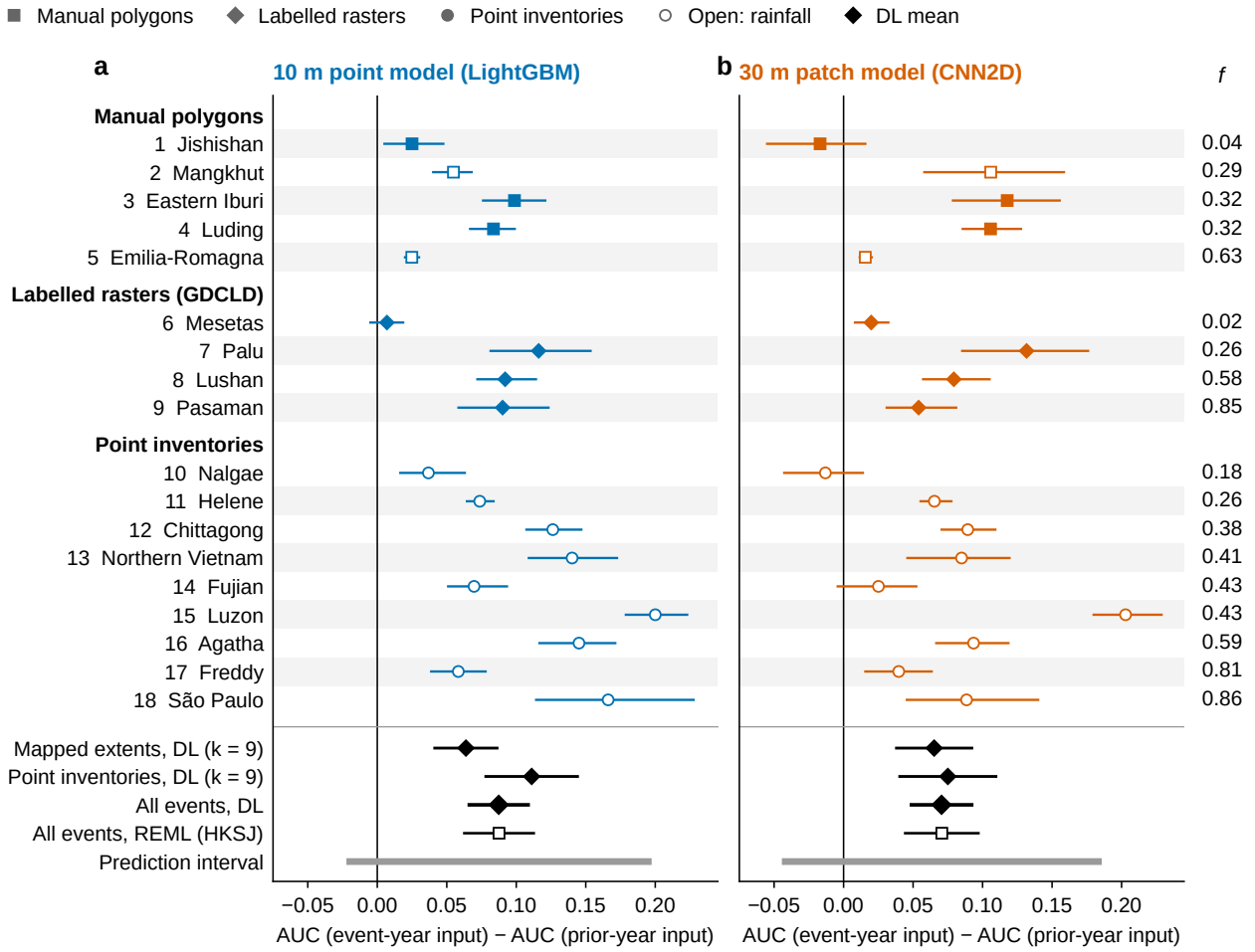


Fig. 2 Event-year AEF increments under fixed spatial validation for **a** the 10 m point model and **b** the 30 m patch model. Rows are events, grouped by inventory form and ordered within groups by the post-event fraction f (right column); marker shape gives the inventory form, and open markers are rainfall events. Markers and whiskers show the paired AUC difference between event-year and prior-year inputs with its 95% spatial-cluster bootstrap interval. Below the events: DerSimonian–Laird (DL) means for each inventory group and for all events, the REML mean with its HKSJ interval and the approximate prediction interval for a new event

Event-year inputs change the top-ranked area of susceptibility maps

Across the nine target-conditioned domains, top-10% capture increased by 22.1 percentage points for the point model (14.8–29.4) and by 20.7 points for the patch model (13.6–27.8). Capture increased in all nine events (Fig. 3a). The smallest changes were comparable to the variation of the map placebo. These are changes in the share of landslide area captured within the same area budget, not changes in overall accuracy.

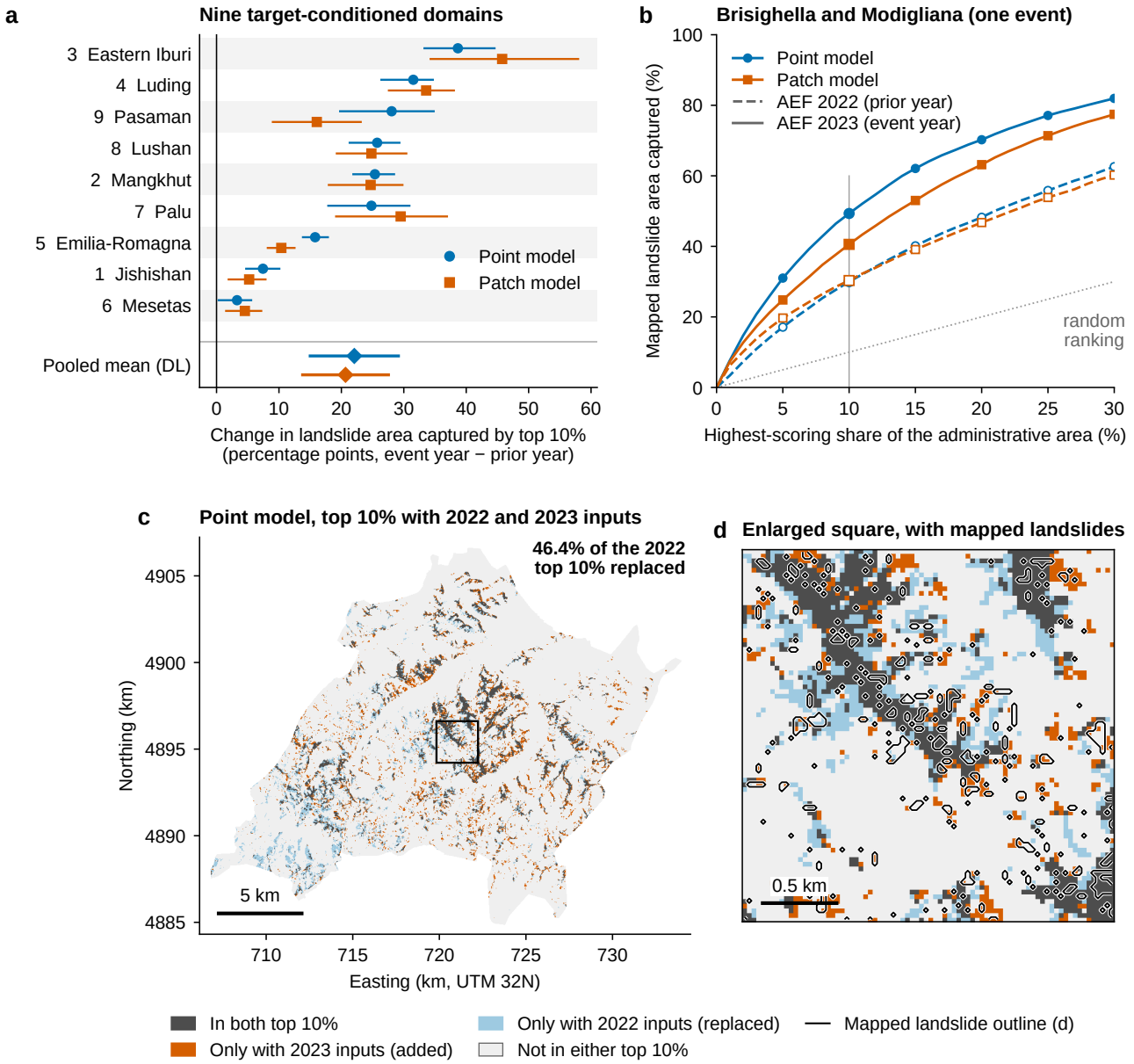


Fig. 3 Map consequences of the input year. **a** Change in top-10% landslide-area capture (event-year minus prior-year input) in nine target-conditioned domains, with DL means. **b** Capture curves over Brisighella and Modigliana (Emilia-Romagna, Italy); markers show capture at 10% of the area, and the dotted line is the expectation under random ranking. **c** Point-model top 10% with prior-year (2022) and event-year (2023) inputs over the administrative grid (WGS 84 / UTM zone 32N, EPSG:32632): cells selected in both years, only with 2022 inputs (replaced) and only with 2023 inputs (added). **d** The 2.4 km square outlined in **c**, centred on the median row and column of the domain, with mapped landslide outlines. Scores average five spatial out-of-fold designs; the 329,953 cells at 30 m represent one event

The administrative domain shows the same direction without a target-proximity restriction (Fig. 3b). Point-model top-10% capture rose from 30.0% with 2022 inputs to 49.3% with 2023 inputs, a gain of 19.3 percentage points (14.3–25.4). Patch-model capture rose from 30.3% to 40.6%, a gain of 10.3 points (5.1–15.4). Average precision rose from 0.074 to 0.150 and from 0.088 to 0.123, at a mapped landslide prevalence of 3.04%. Within the point model's top 10%, the mapped landslide share of the selected area rose from 9.1% to 15.0%.

The top-ranked area itself moved (Fig. 3c, d; Table S24). For the point model, the event-year layer replaced 46.4% (41.0–51.2%) of the prior-year top 10%, and the two selections overlapped with J = 0.366 (0.323–0.418). Between the pre-event layers of 2021 and 2022, 27.7% was replaced (J = 0.566, 0.539–0.594), and the difference

in J was 0.200 (0.159–0.238). The newly selected cells had a mapped landslide share of 15.0%, about five times the domain prevalence, whereas the cells they replaced had 2.3%. The added cells held 22.8% of the mapped landslide area and the replaced cells 3.5%; the difference is the 19.3-point capture gain. The patch model replaced 42.7% (37.6–48.6%), against 29.2% between the pre-event layers (difference in J 0.147, 0.084–0.195). The same ordering held at the 5% and 20% budgets and in each of the five spatial designs.

Observation timing changes discrimination at a fixed number of dates

At Eastern Iburi, the five-cutoff support contains 474 landslide objects and 1,008 controls. The mean three-date AUC rose from 0.453 for the window ending 1 day before the event to 0.791 for the window ending 60 days after it. The increment was +0.337 (+0.289 to +0.380), and with all valid dates +0.391 (+0.325 to +0.450) (Fig. 4a). On the four-endpoint support (281 landslides and 972 controls), the 2018 change was +0.390 and the 2017 change −0.032. The excess over the preceding season was +0.423 (+0.353 to +0.479) (Fig. 4c).

At Mangkhut (1,080 landslide objects and 2,089 controls), the three-date AUC rose from 0.472 to 0.766, an increment of +0.293 (+0.258 to +0.329). The all-date increment was +0.345 (+0.305 to +0.390) (Fig. 4b). On the four-endpoint support (315 landslides and 442 controls), the 2018 change was +0.311 and the 2017 change +0.080, an excess of +0.231 (+0.164 to +0.293) (Fig. 4d).

Within-fold comparisons also gave positive seasonal excesses, 0.335 (0.255–0.402) at Iburi and 0.191 (0.117–0.260) at Mangkhut. Under this metric the 2018 −1-day AUC at Iburi is 0.551, against 0.420 for pooled out-of-fold scores. Absolute pre-event levels thus depend on which sample pairs are compared, whereas the excess stays positive (Table S20). These results concern separability on the stated optical supports, and Mangkhut retains its mixed inventory dates.

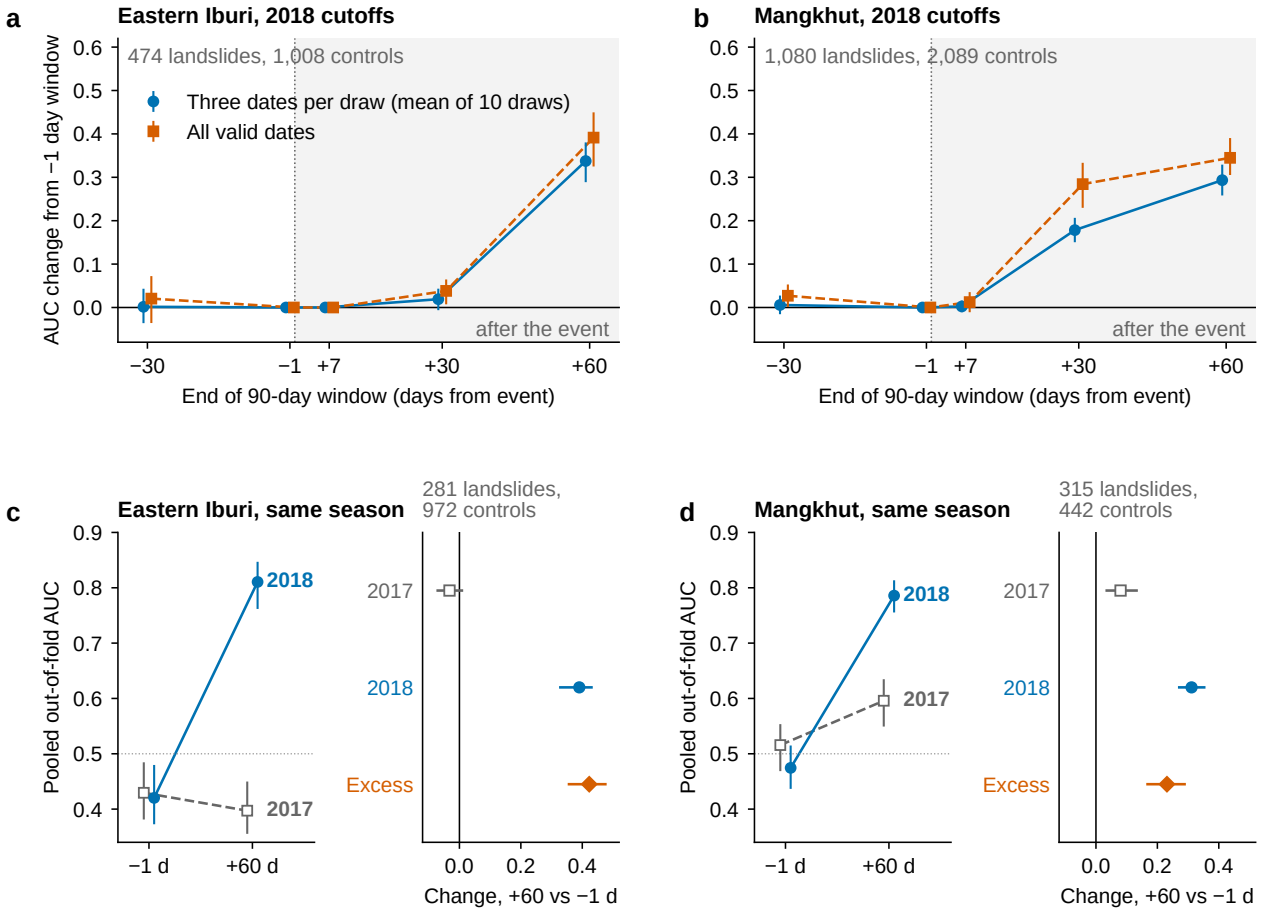


Fig. 4 Controlled Sentinel-2 observation timing. **a, b** AUC change relative to the window that ends 1 day before the event, for 90-day windows ending at five offsets, on each event's five-window support; the shaded area lies after the event. Circles average ten separately evaluated three-date draws, and squares use all valid dates. **c, d** Four-endpoint support. Left: pooled out-of-fold AUC at −1 and +60 days in the event year (2018) and the preceding year (2017); the dotted line marks AUC = 0.5. Right: the +60 minus −1 day change in each year and their difference (excess over 2017). Intervals combine paired spatial-cluster and date-draw resampling; absolute AUCs are listed in Tables S7 and S20

The effect depends on the workflow and appears in other products

The training-year × prediction-year experiment places most of the inflation in the matched use of event-year inputs for training and testing (Fig. 5). Changing only the prediction inputs gave a pooled point effect of 0.0006 (−0.011 to 0.013), with event-specific effects from −0.068 to 0.052; the patch mean was −0.011 (−0.027 to 0.006). Training on event-year inputs and testing on pre-event inputs reduced AUC by 0.043 (point) and 0.053 (patch). The interaction was positive in every event and exceeds the joint increment because it offsets this training-only loss. Event-related surface information is therefore most useful to a model when training and test locations share the same temporal state.

The effect also appears in other annual products. On ten matched point sets, the TESSERA increment was 0.104 (0.073–0.135), against 0.071 (0.047–0.094) for AEF. The TESSERA placebo was not equivalent to zero within ±0.01, and Fig. S2 gives the version-specific contrasts. Annual Sentinel-2 point composites were rebuilt with asset scaling that accounts for harmonization. They gave a mean increment of 0.121 (0.052–0.190) across 15 events, with increases and decreases among single events (Table S5). Treating unresolved harmonization offsets as already applied gave 0.128 (0.057–0.200); Nalgae, where five of 12 event-year scenes remain unresolved, changed from −0.061 to +0.004. Across events, the increment rose with the post-event fraction f. Recovery-

adjusted fits gave half-saturation estimates around 0.23–0.26; several fits are uncertain, and Mangkhut departs from the common response (Online Resource 1, Text S5 and Table S14).

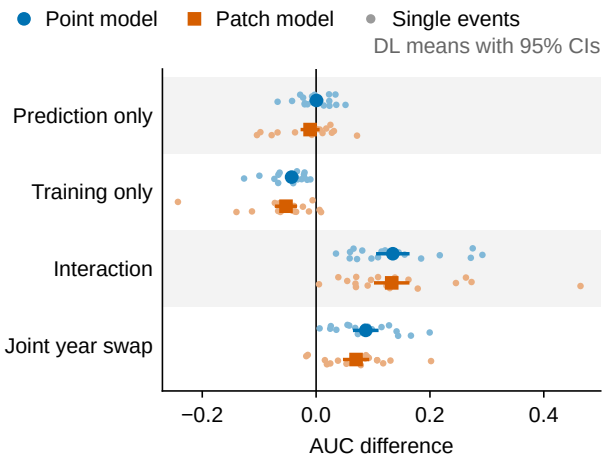


Fig. 5 Training-year × prediction-year components across 18 events. Large markers are DL means with 95% CIs, and small dots are single events. Components add at event level, but separately pooled means use different weights

Pre-target embeddings add region-dependent value beyond landslide history

In North Carolina, conventional factors reached an AUC of 0.726, history alone 0.585 and prior-year AEF alone 0.774 (Fig. 6a). Adding history to the factors gave 0.697, a paired change of −0.030 (−0.065 to +0.001). Adding AEF to this historical baseline gave 0.756, a further +0.059 (+0.044 to +0.077). Factors plus AEF reached 0.777, which is +0.051 (+0.033 to +0.067) above factors alone.

In Lushan, conventional factors reached 0.568, history alone 0.724 and prior-year AEF alone 0.594 (Fig. 6b). Adding history to the factors gave 0.728, a change of +0.160 (+0.070 to +0.238). Adding AEF to this baseline gave 0.736, a further +0.008 (−0.007 to +0.022). Factors plus AEF reached 0.600, or +0.032 (−0.026 to +0.081) above factors alone. The earlier uniform 30 m history exclusion gave a similarly small embedding increment (Table S11).

With the B2 model fixed, substituting event-year AEF at prediction changed AUC by +0.056 (+0.042 to +0.069) in North Carolina and by +0.119 (+0.097 to +0.142) in Lushan. These diagnostics measure how a model trained on earlier landslides responds to post-event input. They need not agree with the 18-event prediction-only component of 0.0006, which was estimated for models trained on the target event itself. Table S11 gives distance-stratified results.

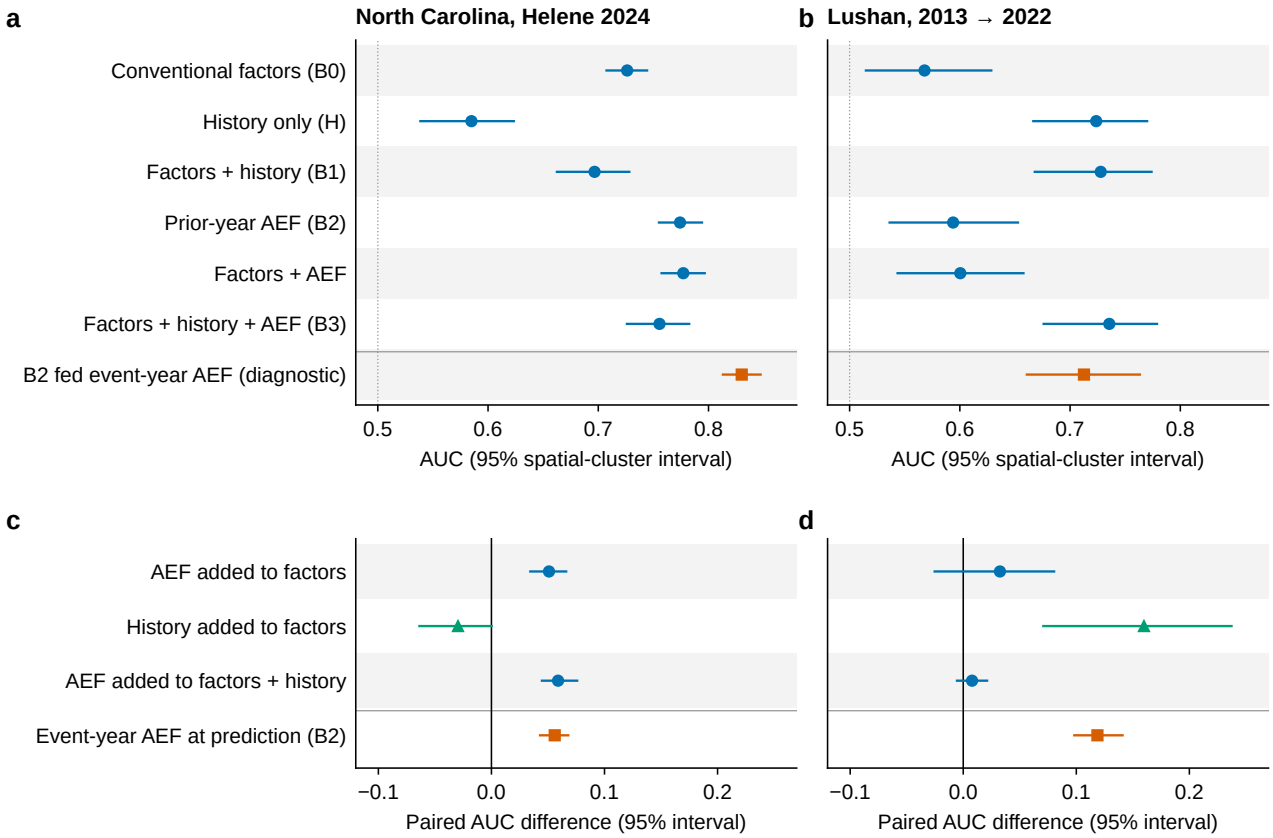


Fig. 6 Retrospective value of pre-target inputs. **a, b** AUC of the six pre-target schemes and of the post-event diagnostic. **c, d** Paired increments against their stated baselines. North Carolina uses 2,711 occurrence-qualified historical records and 5,422 controls generated from those records alone; Lushan uses the 2013 inventory for the 2022 target. Intervals are paired spatial-cluster intervals conditional on the fitted models

Discussion

When within-event validation overstates the ability to anticipate landslides

Annual embeddings describe the land surface in detail, and that detail includes the aftermath of the event being evaluated. In this collection the event-year layer raised AUC by about 0.07–0.09 and moved about a fifth of the mapped landslide area into the top tenth of a map. The administrative maps show how this happens. Almost half of the prior-year top decile was replaced, and the added cells lay on mapped landslides far more often than the cells they replaced. A susceptibility map built this way partly maps the event on which it is evaluated. That is useful for post-event mapping (Behling et al. 2014; Scheip and Wegmann 2021), but it is not evidence that the event could have been anticipated.

The audit adds a condition on the predictors to existing evaluation practice. Spatial blocking controls dependence between training and test locations (Brenning 2005; Roberts et al. 2017). Chrono-validation controls the order of the labels (Lombardo and Tanyas 2020), and evaluation against later events tests a map after its creation (Pareek et al. 2025). None of these designs excludes post-event observations when the predictors are annual layers. Steger et al. (2020) examined a related issue for post-failure topography; annual embeddings extend it to learned multisensor descriptions in which single acquisitions cannot be inspected. The issue concerns the timing of information rather than a particular representation, since the rebuilt Sentinel-2 composites and TESSERA showed it as well.

Post-event surface change, season and regional differences

The optical experiments show that discrimination changes when the observation window moves past the event, even with the number of valid dates fixed. The excess over the preceding season also stays positive. The workflow decomposition adds that event-year training and testing share information that transfers poorly back to the pre-event surface. Together these results point to post-event surface change as an important source of the apparent gain; landslide scars, canopy removal and exposed ground are plausible contributors. The independent Emilia-Romagna disturbance diagnostic also found higher event-year scores at river-bank and field damage. There, the disturbance-versus-undisturbed AUC rose from 0.70 to 0.75 (Online Resource 1, Text S5), so the shared signal can include broader surface disturbance. Because AEF vectors aggregate several sensor streams, the optical test is a controlled input experiment, not a measurement of the encoder's internal weighting.

The size of the effect varied between events, and the prediction intervals for a new event include small and negative values. The year-after signal decays by roughly a quarter per year (recovery ratios 0.770 and 0.762; Online Resource 1, Text S5). This is consistent with gradual revegetation of landslide scars (Yunus et al. 2020). Cloud availability, product construction and recovery differ between regions. The actual observation dates of a product say more than the day of year of the event, and a universal calendar threshold would be inappropriate.

Using historical landslides and pre-event embeddings

The retrospective tests address the information that exists before a target. In North Carolina, conventional factors plus pre-target AEF gave the highest tested pre-target discrimination, and AEF added 0.059 AUC beyond factors and history. In Lushan, explicit history supplied most of the improvement and left a small embedding increment whose interval included zero. Landslide occurrence can depend on earlier landslides (Samia et al. 2017, 2020), so history-based features have value of their own. The history-only model also shows whether a weak fusion result reflects missing historical signal or poor transfer. The regional difference can reflect trigger conditions, the composition and density of the historical inventories, sampling and surface change; the present design cannot attribute it to one of these. Proximity to earlier records within 100 m does not show that the same slope failed again.

The conventional baseline contains terrain, land-cover, hydrological and climatic variables but no lithology or roads (Table 2). The added value of embeddings is therefore measured against this baseline, not against a complete engineering-geological model. Bryce et al. (2025) updated a susceptibility model for Scotland with a larger inventory, slope units and uncertainty estimates, and considered how to communicate that uncertainty with the predictions. Claims of added value from embeddings need the same explicit statement of baseline, mapping unit and domain.

Inventories, evaluation domains and deployment conditions

The evidence spans 18 heterogeneous events and three inventory types, which differ in completeness and mapping method (Guzzetti et al. 2012). The point inventories have no survey boundaries, and some evaluation domains depend on target locations, so controls are sampled terrain rather than verified stable ground. Training used crown proxies, whereas map capture counted complete landslide areas, and the position sampled within a landslide can change the fitted model (Ersayin 2026). Mangkhut contains mixed occurrence dates; excluding points within 500 m or 1 km of mapped mining areas (Maus et al. 2022) left its event-year increments positive

(Table S17).

The optical seasonal comparisons retain 25.5% and 28.6% of the initial Iburi and Mangkhut landslide objects. The median slope of retained Iburi landslides is 18.7°, against 22.3° for excluded ones, whereas Mangkhut slopes are similar (31.6° and 31.7°). Controls shift toward gentler slopes at both events (Table S22). At Mangkhut, WorldCover 2021 classifies 74.6% of the retained and 51.8% of the excluded landslide samples as tree cover (Iburi: 66.2% and 71.3%). This layer describes the surface three years after the 2018 events. It cannot reconstruct the pre-event vegetation, and it does not show whether the optical effect is overestimated or underestimated.

North Carolina training controls depend only on occurrence-qualified history, but the confirmation dates of the released inventory are not established, and Lushan keeps a target-based spatial split. Encoder training cutoffs are not documented, and AEF was released after every target event. The retrospective tests therefore show what pre-target observations contain, not that a forecast could have been issued at the time. The administrative test covers two municipalities of one event, and the maps are susceptibility rankings, not hazard or risk maps. Table 3 lists the information that a temporal audit should record and how this study met each item.

Table 3 Information to record when annual satellite products enter a landslide susceptibility assessment

Item	What to record	In this study
Target	Event, region, and whether initiation points or complete landslide areas are evaluated	18 events; crown proxies or reported points for training; complete areas for map capture
Observation cutoff	Observation window of every input, not only its year label	Annual layers Y−2 to Y+2; three-date Sentinel-2 windows ending −30 to +60 days
Inventory chronology	Occurrence date, confirmation date and source of training records	Occurrence-qualified USLI records and the 2013 Lushan inventory; confirmation dates unknown
Product availability	Release of products and encoders, and known training cutoffs	AEF released 30 July 2025; encoder training cutoffs unknown
Spatial design	Folds, buffers and the data used to fit preprocessing	Spatial k-means folds with 500 m buffers; fold-wise imputation checked at Mangkhut
Evaluation domain	Survey, administrative or target-conditioned boundary	Nine target-conditioned domains; two municipalities
Added value	Paired increments over conventional and historical baselines, with uncertainty	Two retrospective tasks; no lithology or roads in the baseline

Conclusions

Annual satellite embeddings can turn the aftermath of a landslide event into apparent susceptibility skill under within-event spatial validation. Across 18 events, event-year AEF inputs raised AUC by 0.0874 for a point model and 0.0705 for a patch model. The average increase survived drift correction and appeared in point inventories and in inventories with mapped extents, although single events varied widely. At a fixed area budget, event-year layers added about 21–22 percentage points of captured landslide area in nine target-conditioned domains. Over two municipalities they replaced 46.4% of the top-ranked area with cells that lay on mapped landslides far more often than the cells they replaced. Pre-target embeddings retained region-dependent value: 0.059 AUC beyond factors and history in North Carolina, and an increment whose interval included zero in Lushan. Landslide susceptibility studies that use annual satellite products should report the observation window of each predictor relative to the target, the chronology of the training inventory and the evaluation domain.

Supplementary information

Online Resource 1: Supplementary Text S1–S6, Tables S1–S24 and Figs. S1–S3 (PDF). Online Resource 2: Supplementary Data S1–S2, the AlphaEarth and TESSERA source files (CSV, zipped). Online Resource 3:

code, compact inputs and outputs of the inventory-form strata and the top-area overlap (zip).

Declarations

Funding No funding was received to assist with the preparation of this manuscript.

Competing interests The authors have no relevant financial or non-financial interests to disclose.

Author contributions Yifan Du: Conceptualization, Methodology, Software, Investigation, Formal analysis, Resources, Visualization, Supervision, Project administration, Writing – original draft, Writing – review & editing. Tianhe Zheng: Investigation. Peiyan Yang: Investigation. Yibo Li: Data curation, Resources. Junhang Zhou: Validation, Formal analysis, Visualization. Kun Yang: Writing – original draft, Writing – review & editing.

Data and code availability Code, the analysis log, per-sample predictions, provenance tables and derived data are archived on Zenodo as Du et al. (2026), version 2.0 (https://doi.org/10.5281/zenodo.23952287; all versions: https://doi.org/10.5281/zenodo.23467611). The archive provides versioned code and environment specifications, per-sample annual and optical predictions, optical date selections and asset metadata, historical-reference and control-sampling records, figure and table inputs, and executable verification entry points. Compact feature matrices allow the retrospective and annual optical models to be refitted without downloading satellite imagery. The inventory-form strata and the top-area overlap added in this version are reproduced by the script, compact inputs and outputs in Online Resource 3. Source-specific acquisition and licence information is included. An earlier version of this manuscript is available as a preprint (https://doi.org/10.31223/X5RB93). The AlphaEarth Foundations Satellite Embedding dataset is produced by Google and Google DeepMind.

References

Abancó C, Jones JN (2023) Areas affected by landslides following Typhoon Mangkhut in Itogon, Philippines, September 2018 [dataset]. NERC EDS Environmental Information Data Centre. https://doi.org/10.5285/32765a61-8510-4df c-b7c7-58bad12f8497

Abancó C, Bennett GL, Matthews AJ, Matera MAM, Tan FJ (2021) The role of geomorphology, rainfall and soil moisture in the occurrence of landslides triggered by 2018 Typhoon Mangkhut in the Philippines. Nat Hazards Earth Syst Sci 21:1531–1550. https://doi.org/10.5194/nhess-21-1531-2021

Bartos M et al (2024) mdbartos/pysheds, version 0.5 [software]. Zenodo. https://doi.org/10.5281/zenodo.3822494

Behling R, Roessner S, Kaufmann H, Kleinschmit B (2014) Automated spatiotemporal landslide mapping over large areas using RapidEye time series data. Remote Sens 6:8026–8055. https://doi.org/10.3390/rs6098026

Belair GM, Jones ES, Luna LV, Mirus BB (2025) Landslide inventories across the United States (ver. 3.0, February 2025) [dataset]. U.S. Geological Survey data release. https://doi.org/10.5066/P14AJF8I

Brenning A (2005) Spatial prediction models for landslide hazards: review, comparison and evaluation. Nat Hazards Earth Syst Sci 5:853–862. https://doi.org/10.5194/nhess-5-853-2005

Brown CF, Kazmierski MR, Pasquarella VJ et al (2025) AlphaEarth Foundations: an embedding field model for accurate and efficient global mapping from sparse label data. arXiv:2507.22291. https://doi.org/10.48550/arXiv.2507.22291

Bryce E, Castro-Camilo D, Dashwood C et al (2025) An updated landslide susceptibility model and a log-Gaussian Cox process extension for Scotland. Landslides 22:517–535. https://doi.org/10.1007/s10346-024-02368-9

Burgi PM, Toney LD, Collins EA et al (2025) Preliminary landslide inventory for landslides triggered by Hurricane Helene (September 2024) [dataset]. U.S. Geological Survey data release. https://doi.org/10.5066/P14CHGKS

Cheng Y, Zhu Q, Fan L (2026) From landslide conditioning factors to satellite embeddings: evaluating the utilisation of Google AlphaEarth for landslide susceptibility mapping using deep learning. arXiv:2601.07268 (v2). https://doi.org/10.48550/arXiv.2601.07268

Daly C, Halbleib M, Smith JI et al (2008) Physiographically sensitive mapping of climatological temperature and precipitation across the conterminous United States. Int J Climatol 28:2031–2064. https://doi.org/10.1002/joc.1688

DerSimonian R, Laird N (1986) Meta-analysis in clinical trials. Control Clin Trials 7:177–188. https://doi.org/10.1016/0197-2456(86)90046-2

Du Y, Zheng T, Yang P, Li Y, Zhou J, Yang K (2026) Code, analysis log and derived data for "Temporal leakage in annual satellite embeddings inflates landslide susceptibility assessments", version 2.0 [dataset]. Zenodo. https://doi.org/10.5281/zenodo.23952287

Ersayin K (2026) The influence of sampling strategies on shallow landslide susceptibility modelling in a mountainous area. Landslides 23:531–546. https://doi.org/10.1007/s10346-025-02646-0

European Space Agency (2022) Copernicus DEM (GLO-30) [dataset]. https://doi.org/10.5270/ESA-c5d3d65

Fang C, Fan X, Wang X et al (2024) A globally distributed dataset of coseismic landslide mapping via multi-source high-resolution remote sensing images. Earth Syst Sci Data 16:4817–4842. https://doi.org/10.5194/essd-16-4817-2024

Fang J, Luo W, Huang Q, Li W, Chen Y-C, Liu C-C (2026) Annual geospatial foundation model embeddings for landslide susceptibility assessment in Taiwan. npj Nat Hazards (in press, published online 16 September 2026). https://doi.org/10.1038/s44304-026-00268-7

Fell R, Corominas J, Bonnard C, Cascini L, Leroi E, Savage WZ (2008) Guidelines for landslide susceptibility, hazard and risk zoning for land use planning. Eng Geol 102:85–98. https://doi.org/10.1016/j.enggeo.2008.03.022

Feng Z, Atzberger C, Jaffer S et al (2025) TESSERA: temporal embeddings of surface spectra for Earth representation and analysis. arXiv:2506.20380. https://doi.org/10.48550/arXiv.2506.20380

Ferrario MF (2023) Inventory of landslides triggered by heavy rainfall in the Emilia-Romagna region (Italy) in May 2023 [dataset]. Zenodo. https://doi.org/10.5281/zenodo.8102429

Ferrario MF, Livio F (2024) Rapid mapping of landslides induced by heavy rainfall in the Emilia-Romagna (Italy) region in May 2023. Remote Sens 16:122. https://doi.org/10.3390/rs16010122

Google DeepMind (2025) AlphaEarth Foundations helps map our planet in unprecedented detail. Official release announcement, 30 July 2025. https://deepmind.google/blog/alphaearth-foundations-helps-map-our-planet-in-unprecedented-detail/. Accessed 1 November 2026

Guzzetti F, Reichenbach P, Ardizzone F, Cardinali M, Galli M (2006) Estimating the quality of landslide susceptibility models. Geomorphology 81:166–184. https://doi.org/10.1016/j.geomorph.2006.04.007

Guzzetti F, Mondini AC, Cardinali M, Fiorucci F, Santangelo M, Chang K-T (2012) Landslide inventory maps: new tools for an old problem. Earth-Sci Rev 112:42–66. https://doi.org/10.1016/j.earscirev.2012.02.001

Hartung J, Knapp G (2001) A refined method for the meta-analysis of controlled clinical trials with binary outcome. Stat Med 20:3875–3889. https://doi.org/10.1002/sim.1009

IntHout J, Ioannidis JPA, Borm GF (2014) The Hartung-Knapp-Sidik-Jonkman method for random effects meta-analysis is straightforward and considerably outperforms the standard DerSimonian-Laird method. BMC Med Res Methodol 14:25. https://doi.org/10.1186/1471-2288-14-25

Jin J, Chen G (2025) The coseismic landslides induced by 2023 Jishishan earthquake [dataset]. Zenodo. https://doi.org/10.5281/zenodo.15791003

Juang CS, Stanley TA, Kirschbaum DB (2019) Using citizen science to expand the global map of landslides: introducing the Cooperative Open Online Landslide Repository (COOLR). PLoS One 14:e0218657. https://doi.org/10.1371/jour

nal.pone.0218657

Kapoor S, Narayanan A (2023) Leakage and the reproducibility crisis in machine-learning-based science. Patterns 4:100804. https://doi.org/10.1016/j.patter.2023.100804

Karasiak N, Dejoux J-F, Monteil C, Sheeren D (2022) Spatial dependence between training and test sets: another pitfall of classification accuracy assessment in remote sensing. Mach Learn 111:2715–2740. https://doi.org/10.1007/s10994-021-05972-1

Kaufman S, Rosset S, Perlich C, Stitelman O (2012) Leakage in data mining: formulation, detection, and avoidance. ACM Trans Knowl Discov Data 6:15. https://doi.org/10.1145/2382577.2382579

Ke G, Meng Q, Finley T et al (2017) LightGBM: a highly efficient gradient boosting decision tree. In: Advances in Neural Information Processing Systems 30, pp 3146–3154

Knezevic J, Atzberger C, Feng Z, Pellegrini AFA, Keshav S, Coomes D (2026) Annual Earth-observation embeddings encode wildfire disturbance and support simplified burned area mapping. arXiv:2609.25731. https://doi.org/10.48550/arXiv.2609.25731

Lakens D (2017) Equivalence tests: a practical primer for t tests, correlations, and meta-analyses. Soc Psychol Personal Sci 8:355–362. https://doi.org/10.1177/1948550617697177

Li M, Li W, Liu H, Liang C (2026) Leveraging geospatial foundation model embeddings for local-scale landslide susceptibility mapping via positive-unlabeled learning. Research Square. https://doi.org/10.21203/rs.3.rs-10786241/v1

Liu H, Xu Y, Hu G et al (2025) Characteristics of earthquake-triggered landslides under high terrain undulation landscapes: a case study of the secondary effects of the 5 September 2022 Ms 6.8 Luding earthquake, SW China. J Geol Soc 182:jgs2024-253. https://doi.org/10.1144/jgs2024-253 (inventory: https://doi.org/10.6084/m9.figshare.28944505.v1)

Liu W, Li S, Shi C, Zhu H, Huang C, Yin L (2026) Landslide mapping and susceptibility assessment in the middle and lower reaches of the Nujiang River (2017–2025) using satellite embedding and multidimensional environmental factors. Remote Sens 18:1854. https://doi.org/10.3390/rs18111854

Lombardo L, Tanyas H (2020) Chrono-validation of near-real-time landslide susceptibility models via plug-in statistical simulations. Eng Geol 278:105818. https://doi.org/10.1016/j.enggeo.2020.105818

Mancino S, Sblano A, Lovergine FP et al (2025) Unified Global Landslide Catalogue (UGLC): a single, standardised global-scale landslide dataset. Earth Syst Sci Data Discuss. https://doi.org/10.5194/essd-2025-482 (dataset: https://doi.org/10.5281/zenodo.18643456)

Maus V, Giljum S, da Silva DM et al (2022) An update on global mining land use. Sci Data 9:433. https://doi.org/10.1038/s41597-022-01547-4 (dataset: https://doi.org/10.1594/PANGAEA.942325)

Merghadi A, Yunus AP, Dou J et al (2020) Machine learning methods for landslide susceptibility studies: a comparative overview of algorithm performance. Earth-Sci Rev 207:103225. https://doi.org/10.1016/j.earscirev.2020.103225

Pareek T, Bhuyan K, van Westen C, Rajaneesh A, Sajinkumar KS, Lombardo L (2025) Analyzing the posterior predictive capability and usability of landslide susceptibility maps: a case of Kerala, India. Landslides 22:655–670. https://doi.org/10.1007/s10346-024-02389-4

Pizziolo M, Berti M, Scaroni M et al (2024) RER2023: the landslide inventory dataset of the May 2023 Emilia-Romagna event, version 1 [dataset]. Zenodo. https://doi.org/10.5281/zenodo.13742643

Ploton P, Mortier F, Réjou-Méchain M et al (2020) Spatial validation reveals poor predictive performance of large-scale ecological mapping models. Nat Commun 11:4540. https://doi.org/10.1038/s41467-020-18321-y

Reichenbach P, Rossi M, Malamud BD, Mihir M, Guzzetti F (2018) A review of statistically-based landslide susceptibility models. Earth-Sci Rev 180:60–91. https://doi.org/10.1016/j.earscirev.2018.03.001

Roberts DR, Bahn V, Ciuti S et al (2017) Cross-validation strategies for data with temporal, spatial, hierarchical, or phy-

logenetic structure. Ecography 40:913–929. https://doi.org/10.1111/ecog.02881

Samia J, Temme A, Bregt A et al (2017) Do landslides follow landslides? Insights in path dependency from a multi-temporal landslide inventory. Landslides 14:547–558. https://doi.org/10.1007/s10346-016-0739-x

Samia J, Temme A, Bregt A, Wallinga J, Guzzetti F, Ardizzone F (2020) Dynamic path-dependent landslide susceptibility modelling. Nat Hazards Earth Syst Sci 20:271–285. https://doi.org/10.5194/nhess-20-271-2020

Scheip CM, Wegmann KW (2021) HazMapper: a global open-source natural hazard mapping application in Google Earth Engine. Nat Hazards Earth Syst Sci 21:1495–1511. https://doi.org/10.5194/nhess-21-1495-2021

Schuirmann DJ (1987) A comparison of the two one-sided tests procedure and the power approach for assessing the equivalence of average bioavailability. J Pharmacokinet Biopharm 15:657–680. https://doi.org/10.1007/BF01068419

Steger S, Schmaltz E, Glade T (2020) The (f)utility to account for pre-failure topography in data-driven landslide susceptibility modelling. Geomorphology 354:107041. https://doi.org/10.1016/j.geomorph.2020.107041

Thasma S, Ho Y-H, Mostafavi A (2026) Beyond backscatter: AlphaEarth land-cover priors for rapid SAR flood segmentation across foundation backbones. arXiv:2606.29134. https://doi.org/10.48550/arXiv.2606.29134

Viechtbauer W (2005) Bias and efficiency of meta-analytic variance estimators in the random-effects model. J Educ Behav Stat 30:261–293. https://doi.org/10.3102/10769986030003261

Xu C, Xu X, Shyu JBH (2015) Database and spatial distribution of landslides triggered by the Lushan, China Mw 6.6 earthquake of 20 April 2013. Geomorphology 248:77–92. https://doi.org/10.1016/j.geomorph.2015.07.002 (inventory: https://doi.org/10.5066/F7KS6Q2P)

Yunus AP, Fan X, Tang X, Jie D, Xu Q, Huang R (2020) Decadal vegetation succession from MODIS reveals the spatio-temporal evolution of post-seismic landsliding after the 2008 Wenchuan earthquake. Remote Sens Environ 236:111476. https://doi.org/10.1016/j.rse.2019.111476

Zanaga D, Van De Kerchove R, Daems D et al (2022) ESA WorldCover 10 m 2021 v200 [dataset]. Zenodo. https://doi.org/10.5281/zenodo.7254221

Zhang S, Li R, Wang F, Iio A (2019) Characteristics of landslides triggered by the 2018 Hokkaido Eastern Iburi earthquake, Northern Japan. Landslides 16:1691–1708. https://doi.org/10.1007/s10346-019-01207-6 (inventory: https://doi.org/10.5281/zenodo.2577300)

Zhu Y, Yin K, Yang H, Zhou C, Wang Z, Liao Y (2026) Temporal validity of landslide inventories in hazard mapping: insights from Hubei Province, China. Landslides 23:417–432. https://doi.org/10.1007/s10346-025-02651-3

Zhuang Y, Hobeichi S, Shi P, Huang F (2026) Evaluating AlphaEarth Foundations embeddings for wildfire susceptibility mapping. arXiv:2608.12663. https://doi.org/10.48550/arXiv.2608.12663

Online Resource 1

Post-event information in annual satellite embeddings inflates the apparent performance of landslide susceptibility models: a paired audit of 18 events

Manuscript submitted to *Landslides*

Yifan Du, Tianhe Zheng, Peiyan Yang, Yibo Li, Junhang Zhou, Kun Yang

Corresponding author: Yifan Du, North China University of Water Resources and Electric Power, 136 Jinshui East Road, Zhengzhou 450046, Henan, China; duyifan619916@gmail.com

Supplementary Text S1–S6, Tables S1–S24 and Figs. S1–S3. Methods precede the principal numerical results and sensitivity analyses. The companion version history records changes to earlier calculations. Tables S19–S22 quantify AUC aggregation, CNN imputation and optical sample composition; Table S5 includes both annual optical scaling rules. Tables S23–S24 and Figs. S2–S3 accompany the inventory-form strata, the top-area overlap and the TESSERA version contrasts reported in the main text. Tables and figure inputs are indexed in `result_index.csv` of the archive. Works cited are listed at the end of this file.

Text S1. Model, sampling and spatial-validation settings

All principal model settings were fixed, without selecting hyperparameters against the target-event test scores. Label 1 denotes a landslide; reported scores are the predicted probability of class 1. Annual input-year comparisons retain the original locations, folds and buffered training masks. New optical comparisons use one point per polygon, so a landslide object cannot cross folds. Controls retain their source sample identity.

For the annual point audit, a 10 m AEF centre vector is used. Spatial KMeans uses 10 folds and 100 bootstrap clusters for Emilia-Romagna and five folds and 30 clusters otherwise (fold seed 0, n_init 5; cluster seed 1, n_init 3). Annual patch eligibility requires valid centre vectors in every compared year and at most 50% cells with a missing channel. The 11 × 11 patches at 30 m aggregate native 10 m cells in 3 × 3 groups. Remaining missing patch values are filled with the channel mean across the retained event-year patches before the spatial split. This label-free imputation uses the retained test-region features in its channel means; normalization thereafter uses only the fitting subset. A scan of all 69 primary event-year arrays records missing values, spatial cells with any missing channel and patches with any missing cell, before and after eligibility. The sensitivity event was selected by the largest retained missing-cell fraction before refitting. Both imputation operators use identical folds, 500 m buffers, inner splits, optimization and three seeds; the stricter operator estimates each channel mean only from the inner fitting subset and applies it to validation and test patches. An absolute change >0.01 in the paired annual increment was the locally specified trigger for considering more events. Table S21 reports the result and the separate archived-model check. The point/patch comparison changes context and resolution as well as architecture.

CNN2D has two 3 × 3 convolution blocks with padding 1: C→2 C and 2 C→4 C channels, each followed by batch normalization, ReLU and 2 × 2 max pooling. Flattened 16 C features enter fully connected layers 16 C→8 C→2 C→2, with ReLU and dropout 0.3 after the first layer. For AEF, C=64. The training-set channel mean and standard deviation (plus 10^{-6}) normalize all subsets. Cross-entropy, Adam, a polynomial learning-rate schedule with power 0.95 over 200 epochs, and early stopping use the settings in Table S1. Each outer fold sets neural seeds to 100 s+k for s=0,1,2 and fold k; predictions are averaged across those three model seeds. The date draws in the optical experiment have a different endpoint: AUC is evaluated before averaging.

Polygon crown proxies are the highest Copernicus GLO-30 DEM cell (European Space Agency 2022) in each

object; raster objects use eight-connected components. Point inventories are deduplicated at 30 m. Polygon controls use the inventory hull plus 1 km; raster controls use the mapping footprint. Both exclude mapped failures and sample slopes >5° at 100–2,000 m from failures. The event provenance table identifies inventories without independent survey footprints. Input validity and spatial-design files in the archive preserve the exact retained audit sample and fold assignment.

For the seven original COOLR events (Agatha, Luzon, northern Vietnam, Chittagong, Freddy, São Paulo and Fujian), exact-date satellite-mapped event records are selected by country and reference date. Exact coordinate duplicates are removed first; a sequential haversine-radius rule then keeps the first point and removes later neighbours within 30 m. One NumPy default_rng(0) stream is shared across the events in that order. For each event, 3 n background candidates select a positive source uniformly with replacement, a distance uniformly on [300, 3,000] m and a bearing uniformly on [0, 2π). Coordinates use local latitude/longitude distance conversion. Candidates must be >200 m from the original event's positive-point tree; sampled controls subsequently require GLO-30 slope >5° and the retained annual-input support. No fixed final control count is imposed on this seven-event branch. The avoidance tree contains that event's mapped points, not an all-event landslide archive. No additional control-to-control deduplication is implemented.

Nalgae uses the same positive deduplication and distance/bearing distributions in a separate seed-0 run. It generates 6 n candidates, with source selection via pandas sampling with replacement (random_state=0), applies >200 m avoidance, slope >5° and finite elevation, then selects up to 2 n controls without replacement (random_state=0). Raster-derived and polygon controls use the separate 100–2,000 m rule above. The original scripts and fixed point designs are preserved; this audit restores their specification without resampling controls. These distributions are uniform in radial distance, not uniform by annular area.

Table S1

Fixed configurations. Unlisted LightGBM settings use the locked library defaults, including binary objective, 20 minimum observations per leaf, no maximum depth, zero L1/L2 penalties, max_bin 255 and no class weighting. Native missing-value handling is available, but current optical and forward matrices are complete; annual patch handling is described above.

Component	Learner/input	Optimization or sampling	Repetition and uncertainty
Annual point audit	LightGBM, 64 AEF components	400 trees; 63 leaves; learning rate 0.05; row/column fractions 0.8; bagging frequency 1; four threads	Seed equals fold index; fixed spatial folds; 1,000 paired cluster resamples
Annual AEF patch audit	CNN2D, 64 × 11 × 11	Adam; initial lr 0.001; batch 512; ≤200 epochs; validation loss improvement 0.0001; patience 10; stratified validation fraction 0.15 of buffered training	Three seeds per fold; mean class-1 probability; fixed fitted models in bootstrap
Corrected annual S2 point audit	Nine median/index features; LightGBM	Same 400-tree point configuration; original 15-event support and folds; actual asset scaling	Per-event paired annual contrasts; 1,000 cluster resamples
Optical cutoffs	Five red/nir/NDVI summaries; LightGBM	400 trees; 63 leaves; lr 0.05; row/column fractions 0.8; model seed 0	Ten three-date draws, seed 0–9; mean AUC; same 1,000 spatial and draw resamples across windows
Optical spatial design	KMeans on projected point coordinates	Five folds, 30 clusters, n_init 10 and seed 1; 500 m exclusion from test points	≥100 per class per support; ≥30 per class in buffered training

Component	Learner/input	Optimization or sampling	Repetition and uncertainty
Retrospective schemes	LightGBM, B0/H/B1/B2/B3/B0+AEF	500 trees; other point parameters unchanged; seed 0; no test tuning	NC:100 clusters; Lushan:30; n_init 3, seed 1; 1,000 cluster resamples
NC training controls	30 m grid; qualified-history hull +1 km	Slope>5°; qualified-history distance>100 m; 2:1 controls; 5 km strata by candidate area; largest-remainder quota; seed 0, without replacement	One frozen control sample used by every scheme; no replacement after feature eligibility

Text S2. Optical assets, information budget and sample selection

The observation universe consists of public HTTPS Sentinel-2 L2A COG assets returned by Earth Search for the fixed point bounding boxes and dates. Scene records distinguish points outside a scene, unavailable non-public assets and successful reads. Network failures are not interpreted as missing observations. Pixel quality requires SCL 4,5,6 or 7, non-nodata red/nir and a positive denominator. Class 7 is unclassified, so "valid date" denotes this mask rather than guaranteed clear sky. These choices apply identically to 2017 and 2018. First-valid-date and exposure summaries refer to this asset universe and mask.

Declared scale/offset and harmonization state are reconciled before conversion. The early zero-offset assets use zero; assets marked as already harmonized also use zero effective offset, avoiding a second subtraction. For one actual harmonized scene in each optical case, 16 red and 16 near-infrared pixels match the corresponding Collection 1 values after its documented offset: the reference DN is exactly 1,000 higher. These checks identify the scaling of the stored values, independently of model performance. The asset manifest records collection, scene ID, processing baseline, product identity, scale/offset, nodata, URLs and catalogue hashes. Selected original SAFE tile metadata and tile-info files cross-check scene identity and processing baseline. The pixel-level checks and original/reference DN values are supplied in radiometric_pixel_checks.csv. Annual nonzero-offset assets without a confirmed harmonization flag are additionally compared with Collection 1 or Planetary Computer reference pixels. A resolution requires at least five valid pairs, median reflectance mismatch ≤ 0.01, 90th-percentile mismatch ≤ 0.02, and agreement between red and near infrared. Unresolved cases retain their declared offset in the principal annual point analysis; a separate sensitivity treats that residual offset as already applied. Neither rule is selected by AUC. This sensitivity reports the effect of the remaining ambiguity, without claiming an absolute radiometric validation of every asset. The quality-count table records how many scene-point observations fail denominator checks or have NDVI clipped. Finite negative reflectance alone is not used as proof of an incorrect asset offset.

Daily medians combine overlapping tiles after the validity mask. A window spans 90 calendar dates inclusively; its reference day is omitted. Date selections are sampled without replacement. For a given draw, all five features use that point's same three dates. A classifier is fit separately for every window and draw. The primary statistic is the mean of ten AUCs or paired AUC contrasts, not the AUC of an averaged prediction. The archive retains both quantities for audit, but the ensemble diagnostic does not enter the fixed-count conclusion. Ten draws can cover more than three dates in total; Table S9 and the per-point selections document that union explicitly.

Spatial bootstrap weights are drawn once per support set (seed 1), identically across all windows and years. Within each spatial resample, ten draw indices are sampled with replacement (seed 2) and the mean paired contrast is computed. Percentile intervals come from that final distribution, never from averaged confidence limits. Space-only and single-draw intervals are supplied as sensitivity measures. Scores and model fits remain fixed during this resampling, so full training uncertainty is not included.

All comparisons start from 1,100 polygon objects and 2,200 controls per event. The source-row mapping verifies a maximum of one positive sample per object. Five-cutoff 2018, four-endpoint two-year and ten-window two-year support sets are stored as separate boolean fields, together with their exact intersections. Sequential sample-flow tables name the applied window at each step. Selection summaries report polygon area, local GLO-30 neighbourhood slope, descriptive WorldCover 2021 class and date counts for retained and excluded locations. WorldCover 2021 v200 (Zanaga et al. 2022) was sampled from the N42E141 and N15E120 source tiles using WGS84 coordinates, the stored geotransforms and native nearest-pixel indices. All 6,600 candidates have valid class codes. Tile URLs, header hashes, pixel indices and sampled blocks are archived. Land-cover summaries report class counts and proportions; class-code medians are not used. These slope/land-cover summaries are not model inputs or eligibility criteria; WorldCover 2021 describes the later surface at selected locations, not the pre-event land cover of the 2018 events. Table S22 gives the selection contrasts. Figure S1 shows the spatial distribution. The former 5% scene gate is evaluated using the corrected reflectance on common eligible points.

Text S3. Historical inputs and training-sample construction

North Carolina's qualified reference library is the 2,711 retained USLI v3 records (Belair et al. 2025). Each source has a USGS_ID, occurrence interval, qualification decision and snapped 30 m location. The training positives are those records; the new controls use only their domain and avoidance mask. The new 5 km stratum table records candidate counts, allocated quotas and the random seed. Static variables are slope, aspect sine/cosine, curvature, 330 m relief, elevation, log contributing area, WorldCover 2021 and PRISM 1991–2020 precipitation (Daly et al. 2008). The DEM hydrology operator matches the earlier training data: pysheds 0.5 (Bartos et al. 2024) pit/depression filling, flat resolution, flow direction and accumulation. Land cover remains numerically encoded as in the original fixed baseline; no target-driven recoding or tuning is introduced.

Lushan uses the 2013 inventory of Xu et al. (2015) after 30 m source deduplication. Original source-row identifiers map exactly to the 10 m cells of positive training samples. No nearest-neighbour radius is used to infer self identity. The complete source library remains available to 2022 queries, including sources excluded from training by the target hull+1 km split. Static factors are the North Carolina list without precipitation. Train and test points retain their original terrain processing scales and hydrology fields.

An own-source index is removed from a training positive's nearest-distance search and its 1 km count. Other independent sources remain even inside 30 m. Test points and training controls have no own-source exclusion. The H model uses these two history variables alone. For controlled sensitivity comparisons, the earlier North Carolina controls are used with identity exclusion and then with the previous uniform 30 m exclusion. The latter also excludes test-near history; it is labelled as the previous operator, not as the main history baseline. Lushan has the same two historical operators and unchanged training labels.

The shared test samples allow paired comparisons between designs. Near/far strata use the unmodified nearest-source distance and apply to both classes. A historical training record's leave-one distance describes within-library clustering, whereas a future target's distance describes event-to-history proximity; the two relationships need not transfer equally. Keeping a genuine earlier source near a target is chronologically admissible and is not test-label leakage.

Text S4. Event-level and map-level inference

The event, rather than an individual landslide, is the unit for cross-region pooling. The primary DerSimonian–Laird summary is retained; REML heterogeneity, HKSJ confidence intervals, approximate t-based prediction intervals (k-2 degrees of freedom) and leave-one-event/country summaries are reported. The new-event prediction intervals cross zero for both main AEF models. Detailed omission estimates are in `event_meta.csv`.

The primary AUC compares all positive–negative pairs after pooling out-of-fold scores. The sensitivity AUC is $\Sigma(n_+ k\ n_k\ AUCk)/\Sigma(n_+ k\ n_k)$, over folds k with both classes. In bootstrap samples, cluster multiplicities determine each fold's positive and negative counts and the weights are recalculated. Folds with zero positive–negative pairs contribute zero weight. Annual sensitivity retains the original 1,000 sampled cluster-index sequences (seed 1); optical sensitivity uses the existing 30-cluster multinomial sequences (seed 1) with jointly resampled date-draw indices (seed 2). Each optical draw is evaluated before averaging. Equal-fold means are point estimates only. Annual event tables distinguish full-sample point estimates from bootstrap-mean inputs to the original DerSimonian–Laird pooling. Models, folds, sample sets and score direction are unchanged. Tables S19–S20 report both estimands; the paired bootstrap conditions on fitted models.

Mapped positives and negatives are disjoint: positives are inventory cells inside the evaluation domain; negatives are its complement inside that domain. Area capture ranks the whole evaluated domain and allocates exactly 5%, 10% or 20%, sharing the boundary score tie proportionally. Average precision uses this same binary label set. Point estimates are computed from exact scores. The 1,000 spatial-cluster bootstrap uses 4,000 score bins; the archive reports its difference from exact point estimates. Administrative maps use five saved spatial out-of-fold designs averaged before evaluation. Full capture curves, valid support, prevalence and map inputs accompany Table S12. The principal annual map comparison uses common product support, not a reconstructed operational coverage mask.

Text S5. Additional mechanism and exposure evidence

The Emilia-Romagna inventory includes independent river-bank and field-damage polygons. At 2,252 sampled disturbance points, 15,000 landslide crowns and 15,000 undisturbed controls, median AEF change (1-cosine similarity) from 2022 to 2023 was 0.074, 0.048 and 0.042; preceding-year changes were 0.024–0.031. A model trained on landslides versus undisturbed controls scored the disturbance points more highly with event-year inputs: disturbance-versus-undisturbed AUC changed from 0.70 to 0.75, and from 0.71 to 0.79 when restricted to slopes 5–35°. The preceding-year comparison was 0.69→0.70. This supports sensitivity to broader surface disturbance; it does not isolate a uniquely landslide-specific encoder feature.

For the cross-event AEF exposure model, event-year and year-after increments share the prior-year baseline. Their joint 2 × 2 covariance comes from paired spatial bootstrap. The likelihood integrates a normally distributed fully post-event increment using 40-node Gauss–Hermite quadrature and relates the event-year increment to a logistic function of calendar post-event fraction, with positive amplitude, half-saturation in (0, 1) and slope-scale in [0.01, 0.5]. Eight Nelder–Mead starts are refined once; half-saturation intervals are profile-likelihood intervals on 0.02–0.80. Fits reaching boundaries retain those bounds.

AEF year-after-next inputs (17 events) estimate recovery ratios 0.770 (0.661–0.854) for points and 0.762 (0.592–0.898) for patches. Exponential recovery rates are approximately 0.26 and 0.27 per year. Adjusting the year-after reference and its covariance yields half-saturation estimates around 0.23 and 0.26. These describe the current event collection and are not safe-cutoff thresholds. The corrected conventional S2 evi-

dence in this version is the annual point audit and the controlled optical experiments. Earlier S2 patch, fixed 12-month and NDVI-derived mechanism estimates used the superseded offset rule and are retained only in the version history, not as current quantitative evidence.

The four-study literature observation is a targeted search dated 10 October 2026, covering annual-embedding use for dated hazards across arXiv, Research Square, ESS Open Archive and journals, followed by citation checks. Three studies had event-overlapping inputs (Cheng et al. 2026; Li et al. 2026; Zhuang et al. 2026); Fang et al. (2026) used previous-year inputs with temporal and spatial holdouts. This small, selected literature sample does not estimate field-wide prevalence. Post-event mapping is a distinct legitimate task. A newly mapped annual inventory label is not necessarily a newly occurring failure, but high AUC alone does not diagnose leakage in another study.

Text S6. Inventory-form strata and top-area overlap

Both analyses use saved results, and their criteria were written in the analysis log before computation. No model was refitted.

Inventory form. The per-event event-year increments and their spatial-cluster bootstrap standard errors are those of Table S2. Events were grouped by the inventory type recorded in the event provenance table. Manual polygons (Jishishan, Mangkhut, Eastern Iburi, Luding and Emilia-Romagna) and labelled GDCLD rasters (Mesetas, Palu, Lushan and Pasaman) form the mapped-extent group (k = 9); the eight COOLR events and Helene form the point group (k = 9). Group means use the DerSimonian–Laird estimator of the primary analysis, with REML and HKSJ intervals as a robustness analysis. The group difference combines the two DL standard errors in quadrature, so that each group keeps its own between-event variance; a REML mixed-effects meta-regression with a group indicator and a Knapp–Hartung t interval on k - 2 degrees of freedom is the robustness analysis. Drift-corrected increments use the paired bootstrap standard errors of d0 - placebo. Trigger groups are shown only to expose the confounding: all nine point inventories are rainfall events, eight of them with offset controls, and seven of the nine mapped-extent inventories are earthquakes. The per-event estimates were reported before this grouping, so the grouping is a descriptive re-summary rather than a blind test.

Top-area overlap. The maps are the five-design means of the saved administrative-domain predictions over the common support of 2021–2024 (329,953 cells at 30 m). At an area budget q, cells that score above the boundary score receive weight 1 and cells tied at the boundary share the remaining budget, so that the weights sum to q times the number of cells, as in the capture curves. Overlap between years a and b is the weighted Jaccard index $J = \Sigma\min(w_a, w_b)/\Sigma\max(w_a, w_b)$, and the replaced share is $R = 1 - \Sigma\min(w_a, w_b)/(q\,n)$. The capture change decomposes exactly into the mapped landslide area of added cells minus that of replaced cells, divided by the total mapped landslide area. Intervals use the 1,000 spatial-cluster multinomial weights of the capture estimates (NumPy default_rng(1)): in each replicate the cluster multiplicities weight the cell areas and the selection is recomputed. The 5% and 20% budgets and the five individual spatial designs were fixed as sensitivity checks before computation. Fig. 3c of the main text and Fig. S3 assign a fractional boundary cell to the class with the larger weight. Online Resource 3 contains the script, compact inputs and outputs.

Current numerical results

Table S2

Per-event results of the AlphaEarth audit (18 events). n.a.: no Y-2 layer, because AEF begins in 2017. Increments are paired AUC differences with spatial-cluster bootstrap 95% CIs. The increments shown are bootstrap means; the ratio d_0/d_1 is the ratio of the full-sample increments, as used by the joint model in Text S5, and is unstable when d_1 is small.

Event	f	Model	AUC Y-1	Event year (Y - Y-1)	Placebo (Y-1 - Y-2)	Year after (Y+1 - Y-1)	Ratio d0/d1
Mesetas (Colombia)	0.02	LightGBM	0.855	+0.007 (-0.006, +0.019)	+0.022 (+0.009, +0.036)	+0.090 (+0.070, +0.111)	0.07
	0.02	CNN2D	0.878	+0.020 (+0.007, +0.033)	+0.010 (-0.005, +0.026)	+0.081 (+0.066, +0.097)	0.25
Jishishan (China)	0.04	LightGBM	0.591	+0.025 (+0.004, +0.048)	+0.020 (+0.008, +0.032)	+0.026 (+0.003, +0.053)	0.99
	0.04	CNN2D	0.734	-0.017 (-0.056, +0.016)	-0.027 (-0.059, -0.002)	+0.039 (+0.011, +0.070)	-0.44
Nalgae, Mindanao (Philippines)	0.18	LightGBM	0.804	+0.037 (+0.016, +0.064)	+0.012 (-0.009, +0.036)	+0.016 (-0.010, +0.045)	2.13
	0.18	CNN2D	0.768	-0.013 (-0.044, +0.015)	+0.031 (+0.004, +0.061)	-0.026 (-0.055, -0.002)	0.61
Helene, southern Appalachians (USA)	0.26	LightGBM	0.815	+0.074 (+0.064, +0.084)	-0.005 (-0.011, +0.001)	+0.126 (+0.109, +0.146)	0.59
	0.26	CNN2D	0.801	+0.065 (+0.055, +0.078)	-0.010 (-0.020, -0.002)	+0.130 (+0.114, +0.148)	0.50
Palu (Indonesia)	0.26	LightGBM	0.720	+0.116 (+0.081, +0.154)	n.a.	+0.258 (+0.214, +0.298)	0.45
	0.26	CNN2D	0.737	+0.132 (+0.085, +0.177)	n.a.	+0.211 (+0.155, +0.260)	0.63
Mangkhut, Itogon (Philippines)	0.29	LightGBM	0.818	+0.055 (+0.039, +0.069)	n.a.	+0.057 (+0.041, +0.072)	0.97
	0.29	CNN2D	0.763	+0.106 (+0.057, +0.159)	n.a.	+0.070 (+0.035, +0.103)	1.52
Eastern Iburi (Japan)	0.32	LightGBM	0.829	+0.099 (+0.075, +0.122)	n.a.	+0.153 (+0.123, +0.190)	0.65
	0.32	CNN2D	0.830	+0.118 (+0.078, +0.156)	n.a.	+0.153 (+0.112, +0.195)	0.77
Luding (China)	0.32	LightGBM	0.757	+0.084 (+0.066, +0.100)	-0.018 (-0.029, -0.008)	+0.136 (+0.109, +0.163)	0.61
	0.32	CNN2D	0.796	+0.106 (+0.085, +0.128)	-0.012 (-0.031, +0.006)	+0.133 (+0.110, +0.159)	0.80
Chittagong (Bangladesh)	0.38	LightGBM	0.808	+0.126 (+0.106, +0.148)	-0.002 (-0.010, +0.007)	+0.103 (+0.082, +0.126)	1.22
	0.38	CNN2D	0.804	+0.089 (+0.070, +0.110)	-0.004 (-0.015, +0.005)	+0.060 (+0.041, +0.080)	1.49
Northern Vietnam	0.41	LightGBM	0.678	+0.140 (+0.108, +0.173)	+0.013 (-0.004, +0.031)	+0.143 (+0.114, +0.182)	0.98
	0.41	CNN2D	0.721	+0.085 (+0.045, +0.120)	+0.027 (-0.017, +0.071)	+0.074 (+0.035, +0.110)	1.14
Fujian (China)	0.43	LightGBM	0.822	+0.070 (+0.050, +0.094)	-0.008 (-0.026, +0.008)	+0.076 (+0.046, +0.114)	0.92
	0.43	CNN2D	0.800	+0.025 (-0.005, +0.053)	-0.014 (-0.047, +0.020)	+0.016 (-0.016, +0.045)	1.52
Luzon (Philippines)	0.43	LightGBM	0.727	+0.200 (+0.178, +0.224)	+0.007 (-0.002, +0.016)	+0.219 (+0.193, +0.247)	0.91
	0.43	CNN2D	0.729	+0.203 (+0.179, +0.230)	+0.001 (-0.008, +0.012)	+0.210 (+0.184, +0.240)	0.97
Lushan (China)	0.58	LightGBM	0.833	+0.092 (+0.071, +0.115)	+0.003 (-0.007, +0.015)	+0.091 (+0.068, +0.115)	1.01
	0.58	CNN2D	0.842	+0.079 (+0.056, +0.106)	-0.003 (-0.014, +0.006)	+0.081 (+0.057, +0.110)	0.98
Agatha (Mexico)	0.59	LightGBM	0.766	+0.145 (+0.116, +0.172)	-0.010 (-0.024, +0.005)	+0.114 (+0.090, +0.137)	1.27
	0.59	CNN2D	0.789	+0.094 (+0.066, +0.119)	-0.010 (-0.030, +0.010)	+0.055 (+0.031, +0.077)	1.70
Emilia-Romagna (Italy)	0.63	LightGBM	0.908	+0.025 (+0.019, +0.031)	+0.000 (-0.004, +0.005)	+0.024 (+0.017, +0.031)	1.04
	0.63	CNN2D	0.935	+0.016 (+0.011, +0.021)	+0.002 (-0.001, +0.006)	+0.017 (+0.012, +0.023)	0.90

Event	f	Model	AUC Y-1	Event year (Y - Y-1)	Placebo (Y-1 - Y-2)	Year after (Y+1 - Y-1)	Ratio d0/d1
Freddy (Malawi)	0.81	LightGBM	0.853	+0.058 (+0.038, +0.079)	+0.009 (+0.000, +0.019)	+0.044 (+0.020, +0.069)	1.33
	0.81	CNN2D	0.833	+0.040 (+0.015, +0.064)	+0.009 (-0.005, +0.024)	+0.028 (+0.011, +0.046)	1.36
Pasaman, West Sumatra (Indonesia)	0.85	LightGBM	0.884	+0.090 (+0.058, +0.124)	+0.005 (-0.005, +0.016)	+0.076 (+0.046, +0.105)	1.18
	0.85	CNN2D	0.907	+0.054 (+0.030, +0.082)	-0.006 (-0.018, +0.004)	+0.037 (+0.019, +0.057)	1.45
São Paulo coast (Brazil)	0.86	LightGBM	0.791	+0.166 (+0.113, +0.228)	-0.022 (-0.043, -0.001)	+0.154 (+0.100, +0.220)	1.08
	0.86	CNN2D	0.798	+0.088 (+0.045, +0.141)	-0.004 (-0.023, +0.018)	+0.065 (+0.036, +0.092)	1.37

Table S3

AEF event-level heterogeneity (between-event standard deviation tau) and prediction intervals. Detailed omission estimates are supplied in the companion CSV.

model	est	lo_hk	hi_hk	tau	pred_lo	pred_hi
LightGBM	0.088	0.062	0.114	0.050	-0.022	0.197
CNN2D	0.071	0.043	0.098	0.053	-0.044	0.186

Current embedding-only pooled contrasts. These analyses are unchanged by the optical scaling correction. Per-event inputs are bootstrap means. TOST evaluates equivalence within ±0.01 AUC; a displayed 0.000 denotes p<0.001; n.a.: equivalence is tested for placebo contrasts only.

Point set	Representation / model	Contrast	k	DerSimonian–Laird (95% CI)	REML with HKSJ interval	Positive events	TOST p (DL / HKSJ)
AlphaEarth, audit points	LightGBM	event year d_0	18	+0.087 (+0.065, +0.110)	+0.088 (+0.062, +0.114)	18/18	n.a.
AlphaEarth, audit points	LightGBM	placebo	15	+0.002 (-0.003, +0.007)	+0.002 (-0.005, +0.009)	9/15	0.001 / 0.011
AlphaEarth, audit points	LightGBM	year after d_1	18	+0.104 (+0.076, +0.133)	+0.105 (+0.072, +0.137)	18/18	n.a.
AlphaEarth, audit points	LightGBM	d_0 - placebo	15	+0.085 (+0.057, +0.113)	+0.085 (+0.051, +0.120)	14/15	n.a.
AlphaEarth, audit points	CNN2D	event year d_0	18	+0.070 (+0.048, +0.093)	+0.071 (+0.043, +0.098)	16/18	n.a.
AlphaEarth, audit points	CNN2D	placebo	15	-0.002 (-0.006, +0.003)	-0.002 (-0.007, +0.003)	6/15	0.000 / 0.002
AlphaEarth, audit points	CNN2D	year after d_1	18	+0.078 (+0.052, +0.104)	+0.078 (+0.047, +0.110)	17/18	n.a.
AlphaEarth, audit points	CNN2D	d_0 - placebo	15	+0.064 (+0.035, +0.093)	+0.064 (+0.031, +0.096)	14/15	n.a.
TESSERA points	TESSERA	event year d_0	10	+0.104 (+0.073, +0.135)	+0.105 (+0.061, +0.149)	10/10	n.a.
TESSERA points	TESSERA	placebo	10	+0.003 (-0.010, +0.016)	+0.003 (-0.015, +0.020)	5/10	0.148 / 0.184
TESSERA points	TESSERA	year after d_1	10	+0.121 (+0.089, +0.154)	+0.121 (+0.091, +0.151)	10/10	n.a.
TESSERA points	TESSERA	d_0 - placebo	10	+0.103 (+0.058, +0.147)	+0.104 (+0.044, +0.163)	9/10	n.a.
TESSERA points	AlphaEarth	event year d_0	10	+0.071 (+0.047, +0.094)	+0.073 (+0.036, +0.109)	10/10	n.a.
TESSERA points	AlphaEarth	placebo	10	-0.002 (-0.010, +0.006)	-0.003 (-0.014, +0.009)	4/10	0.030 / 0.089
TESSERA points	AlphaEarth	year after d_1	10	+0.088 (+0.055, +0.121)	+0.088 (+0.052, +0.123)	10/10	n.a.
TESSERA points	AlphaEarth	d_0 - placebo	10	+0.072 (+0.044, +0.101)	+0.075 (+0.028, +0.122)	9/10	n.a.

Table S4

TESSERA audit (10 events) with AlphaEarth recomputed on the same points, folds and bootstrap resamples.

Event	f	TESSERA version	Points (ls / all)	Pre-event AUC TESSERA / AE	TESSERA event year	TESSERA placebo	TESSERA year after	AlphaEarth event year	AE - TESSERA (event year)
Mesetas (Colombia)	0.02	v1	1,990 / 5,970	0.754 / 0.855	+0.020 (-0.002, +0.044)	+0.041 (+0.023, +0.062)	+0.127 (+0.095, +0.158)	+0.006 (-0.006, +0.019)	-0.014 (-0.035, +0.008)
Jishishan (China)	0.04	v1	2,984 / 8,660	0.537 / 0.541	+0.048 (+0.010, +0.080)	+0.016 (-0.001, +0.030)	+0.082 (+0.017, +0.148)	+0.020 (+0.000, +0.041)	-0.028 (-0.050, -0.002)
Helene, southern Appalachians (USA)	0.26	v1	2,213 / 6,639	0.706 / 0.815	+0.114 (+0.087, +0.154)	-0.007 (-0.022, +0.009)	+0.175 (+0.144, +0.214)	+0.073 (+0.064, +0.084)	-0.041 (-0.078, -0.013)
Luding (China)	0.32	v1	2,675 / 7,859	0.630 / 0.705	+0.066 (+0.047, +0.086)	+0.030 (+0.004, +0.050)	+0.144 (+0.102, +0.182)	+0.086 (+0.066, +0.102)	+0.019 (-0.000, +0.037)
Fujian (China)	0.43	v1	345 / 1,036	0.748 / 0.822	+0.125 (+0.087, +0.168)	-0.029 (-0.067, +0.006)	+0.107 (+0.074, +0.145)	+0.069 (+0.050, +0.094)	-0.056 (-0.100, -0.015)
Lushan (China)	0.58	v1	1,286 / 3,858	0.763 / 0.833	+0.113 (+0.092, +0.138)	-0.023 (-0.042, -0.004)	+0.103 (+0.081, +0.130)	+0.091 (+0.071, +0.115)	-0.022 (-0.042, -0.001)
Agatha (Mexico)	0.59	v1.1-cam	2,949 / 5,213	0.685 / 0.749	+0.182 (+0.148, +0.218)	-0.006 (-0.020, +0.008)	+0.165 (+0.137, +0.197)	+0.159 (+0.126, +0.197)	-0.023 (-0.053, +0.007)
Emilia-Romagna (Italy)	0.63	v1	3,000 / 9,000	0.814 / 0.897	+0.062 (+0.050, +0.075)	+0.011 (-0.004, +0.023)	+0.049 (+0.037, +0.063)	+0.031 (+0.023, +0.039)	-0.031 (-0.045, -0.020)
Freddy (Malawi)	0.81	v1.1-cam	1,634 / 4,582	0.735 / 0.853	+0.118 (+0.088, +0.143)	+0.011 (-0.010, +0.029)	+0.097 (+0.068, +0.122)	+0.058 (+0.038, +0.079)	-0.060 (-0.082, -0.035)
São Paulo coast (Brazil)	0.86	v1.1-cam	326 / 717	0.712 / 0.791	+0.227 (+0.171, +0.284)	-0.037 (-0.068, -0.000)	+0.173 (+0.118, +0.229)	+0.167 (+0.113, +0.228)	-0.060 (-0.108, -0.017)

Table S5

Annual Sentinel-2 point composites under the two asset-scaling rules. Original 15-event samples, folds and learner settings are fixed. The primary rule applies the declared offset only where harmonization is unresolved; the alternative treats those unresolved offsets as already applied. Other assets are identical. Changes are event-year minus prior-year AUC; intervals use the same 1,000 spatial-cluster resamples. The last contrast subtracts the primary increment from the alternative increment. Negative effects remain in pooling. Scene-point fractions describe optical sampling, not foundation-model information weights.

Event	Primary AUC prior / event	Primary change (95% CI)	Alternative change (95% CI)	Alternative - primary (95% CI)	Positive / control
Chittagong	0.559 / 0.862	+0.304 (+0.269, +0.342)	+0.332 (+0.301, +0.362)	+0.028 (+0.008, +0.047)	448 / 896
São Paulo	0.285 / 0.784	+0.499 (+0.326, +0.667)	+0.494 (+0.321, +0.664)	-0.005 (-0.040, +0.031)	82 / 89
Fujian	0.602 / 0.749	+0.147 (+0.037, +0.259)	+0.149 (+0.063, +0.247)	+0.002 (-0.043, +0.046)	91 / 182
Agatha	0.543 / 0.625	+0.081 (+0.022, +0.140)	+0.068 (+0.005, +0.128)	-0.014 (-0.055, +0.023)	964 / 733
Freddy	0.554 / 0.693	+0.139 (+0.063, +0.203)	+0.139 (+0.063, +0.203)	+0.000 (+0.000, +0.000)	523 / 862
Nalgae (Mindanao)	0.522 / 0.461	-0.061 (-0.165, +0.065)	+0.004 (-0.116, +0.175)	+0.065 (-0.058, +0.203)	56 / 112
Luzon	0.547 / 0.757	+0.209 (+0.184, +0.237)	+0.202 (+0.179, +0.225)	-0.008 (-0.027, +0.013)	806 / 1613
Northern Vietnam	0.540 / 0.714	+0.173 (+0.127, +0.214)	+0.177 (+0.130, +0.220)	+0.004 (-0.019, +0.027)	562 / 1055
Lushan	0.628 / 0.779	+0.151 (+0.095, +0.208)	+0.155 (+0.098, +0.212)	+0.004 (-0.018, +0.029)	437 / 517
Mesetas	0.565 / 0.478	-0.088 (-0.160, -0.001)	-0.088 (-0.160, -0.001)	+0.000 (+0.000, +0.000)	472 / 620
Palu	0.442 / 0.607	+0.165 (+0.089, +0.238)	+0.165 (+0.089, +0.238)	+0.000 (+0.000, +0.000)	332 / 677
Pasaman	0.509 / 0.732	+0.223 (+0.113, +0.317)	+0.225 (+0.113, +0.323)	+0.001 (-0.019, +0.023)	100 / 219
Eastern Iburi	0.386 / 0.433	+0.047 (+0.015, +0.080)	+0.047 (+0.015, +0.080)	+0.000 (+0.000, +0.000)	2008 / 3501
Luding	0.551 / 0.519	-0.032 (-0.072, +0.003)	-0.027 (-0.069, +0.010)	+0.005 (-0.005, +0.017)	2098 / 3834
Emilia-Romagna	0.710 / 0.646	-0.064 (-0.100, -0.027)	-0.042 (-0.076, -0.009)	+0.022 (+0.010, +0.033)	3000 / 5997

Nalgae's point estimate crosses zero, but its paired difference interval crosses zero too. In that event, 5/12 selected 2022 scenes are unresolved and supply 460/1,289 (35.7%) valid scene-point observations on the fixed sample support; both pre-event years and 2023 have no unresolved scenes. Across all events and years, the scene and observation denominators are in annual_s2_unresolved_exposure.csv, with scene identities and local raw-chunk hashes in annual_s2_observation_sources.csv.

Table S6

Optical common-support counts. Each event starts with 1,100 positive objects and 2,200 controls. The companion flow table records every sequential exclusion and the set-intersection table verifies which populations overlap; ratios between different support sets are not reported as retention rates.

event	subset	n_pos	n_neg	status
IBU2018	curve	474	1008	estimated
IBU2018	curve_all	474	1008	estimated
IBU2018	season	281	972	estimated
IBU2018	allten	0	0	ineligible: class below 100
IBU2018	gate	489	1291	estimated
MKH2018	curve	1080	2089	estimated
MKH2018	curve_all	1080	2089	estimated
MKH2018	season	315	442	estimated
MKH2018	allten	225	326	estimated
MKH2018	gate	1079	2101	estimated

Table S7

Absolute AUC for all four seasonal endpoints. Main AUC averages independently evaluated three-date draws; its 95% interval uses joint spatial and draw resampling. Seed 0 is the single fixed-three-date-set sensitivity. Fold-level scores and AUCs, including values below 0.5, are archived without score reversal. Other optical tables use IBU 2018 for Eastern Iburi and MKH 2018 for Mangkhut.

Event	Year / cutoff	Mean AUC	CI lower	CI upper	Seed-0 AUC	Landslides	Controls
Eastern Iburi	2017 / -1 d	0.429	0.381	0.485	0.394	281	972
Eastern Iburi	2017 / 60 d	0.397	0.355	0.450	0.401	281	972
Eastern Iburi	2018 / -1 d	0.420	0.373	0.480	0.460	281	972
Eastern Iburi	2018 / 60 d	0.811	0.762	0.847	0.819	281	972
Mangkhut	2017 / -1 d	0.516	0.469	0.554	0.509	315	442
Mangkhut	2017 / 60 d	0.596	0.549	0.635	0.586	315	442
Mangkhut	2018 / -1 d	0.475	0.437	0.515	0.459	315	442
Mangkhut	2018 / 60 d	0.786	0.755	0.814	0.767	315	442

Table S8

Optical paired contrasts. The scene-gate difference is computed on the same eligible points and compares the gated with the pixel-only cutoff increment. The allten rows, where eligible, use their own support.

event	subset	contrast	effect_95CI	seed0
IBU2018	curve	y2018_d-30-y2018_d-1	+0.002 (-0.036 to +0.043)	0.000
IBU2018	curve	y2018_d7-y2018_d-1	+0.000 (+0.000 to +0.000)	0.000
IBU2018	curve	y2018_d30-y2018_d-1	+0.019 (-0.006 to +0.043)	-0.017
IBU2018	curve	y2018_d60-y2018_d-1	+0.337 (+0.289 to +0.380)	0.329
IBU2018	curve_all	y2018_d-30-y2018_d-1	+0.020 (-0.036 to +0.072)	0.020
IBU2018	curve_all	y2018_d7-y2018_d-1	+0.000 (+0.000 to +0.000)	0.000
IBU2018	curve_all	y2018_d30-y2018_d-1	+0.038 (+0.007 to +0.065)	0.038
IBU2018	curve_all	y2018_d60-y2018_d-1	+0.391 (+0.325 to +0.450)	0.391
IBU2018	season	y2017_d60-y2017_d-1	-0.032 (-0.075 to +0.012)	0.007
IBU2018	season	y2018_d60-y2018_d-1	+0.390 (+0.324 to +0.434)	0.359
IBU2018	season	DID_d60	+0.423 (+0.353 to +0.479)	0.352
IBU2018	gate	y2018_d60-y2018_d-1	+0.338 (+0.281 to +0.384)	0.318
IBU2018	gate	y2018_d60_gate-y2018_d-1_gate	+0.339 (+0.283 to +0.388)	0.342
IBU2018	gate	gate_change_in_event_increment	+0.001 (-0.017 to +0.019)	0.023
MKH2018	curve	y2018_d-30-y2018_d-1	+0.006 (-0.015 to +0.027)	0.035
MKH2018	curve	y2018_d7-y2018_d-1	+0.002 (-0.011 to +0.016)	0.023
MKH2018	curve	y2018_d30-y2018_d-1	+0.178 (+0.150 to +0.207)	0.210
MKH2018	curve	y2018_d60-y2018_d-1	+0.293 (+0.258 to +0.329)	0.315
MKH2018	curve_all	y2018_d-30-y2018_d-1	+0.027 (+0.001 to +0.053)	0.027
MKH2018	curve_all	y2018_d7-y2018_d-1	+0.012 (-0.011 to +0.035)	0.012
MKH2018	curve_all	y2018_d30-y2018_d-1	+0.284 (+0.230 to +0.333)	0.284
MKH2018	curve_all	y2018_d60-y2018_d-1	+0.345 (+0.305 to +0.390)	0.345
MKH2018	season	y2017_d60-y2017_d-1	+0.080 (+0.031 to +0.136)	0.077
MKH2018	season	y2018_d60-y2018_d-1	+0.311 (+0.267 to +0.357)	0.308
MKH2018	season	DID_d60	+0.231 (+0.164 to +0.293)	0.231
MKH2018	allten	y2017_d-30-y2017_d-1	+0.012 (-0.027 to +0.048)	-0.014
MKH2018	allten	y2017_d7-y2017_d-1	-0.016 (-0.047 to +0.017)	-0.039
MKH2018	allten	y2017_d30-y2017_d-1	-0.041 (-0.086 to +0.006)	-0.120
MKH2018	allten	y2017_d60-y2017_d-1	+0.085 (+0.030 to +0.138)	0.046
MKH2018	allten	y2018_d-30-y2018_d-1	+0.031 (-0.008 to +0.071)	0.051
MKH2018	allten	y2018_d7-y2018_d-1	+0.017 (-0.021 to +0.062)	0.021
MKH2018	allten	y2018_d30-y2018_d-1	+0.193 (+0.146 to +0.242)	0.149
MKH2018	allten	y2018_d60-y2018_d-1	+0.321 (+0.271 to +0.370)	0.277
MKH2018	allten	DID_d-30	+0.020 (-0.043 to +0.087)	0.065
MKH2018	allten	DID_d7	+0.033 (-0.019 to +0.091)	0.060
MKH2018	allten	DID_d30	+0.234 (+0.170 to +0.294)	0.269
MKH2018	allten	DID_d60	+0.236 (+0.170 to +0.308)	0.231
MKH2018	gate	y2018_d60-y2018_d-1	+0.295 (+0.265 to +0.327)	0.320
MKH2018	gate	y2018_d60_gate-y2018_d-1_gate	+0.297 (+0.266 to +0.333)	0.308
MKH2018	gate	gate_change_in_event_increment	+0.002 (-0.013 to +0.016)	-0.011

Table S9

Distinct dates in the union of ten current draws, among all points individually eligible in each window. Each draw uses exactly three dates and is evaluated separately. Counts describe the date pool across draws, not a single prediction's information budget. The superseded prediction-ensemble date audit is retained in the versioned data files.

Event	Window	Points	Minimum	Median	Maximum
IBU2018	y2017_d-1	2761	3	3.000	5
IBU2018	y2017_d30	465	3	3.000	4
IBU2018	y2017_d60	2140	3	3.000	6
IBU2018	y2017_d7	2761	3	3.000	5
IBU2018	y2018_d-1	1876	3	3.000	6
IBU2018	y2018_d-30	2369	3	3.000	6
IBU2018	y2018_d30	2132	3	4.000	7
IBU2018	y2018_d60	3027	3	5.000	9
IBU2018	y2018_d7	1876	3	3.000	6
MKH2018	y2017_d-1	3006	3	4.000	8
MKH2018	y2017_d-30	3158	3	5.000	10
MKH2018	y2017_d30	1293	3	3.000	6
MKH2018	y2017_d60	812	3	3.000	5
MKH2018	y2017_d7	2405	3	4.000	7
MKH2018	y2018_d-1	3181	3	6.000	14
MKH2018	y2018_d-30	3249	3	7.000	16
MKH2018	y2018_d30	3279	3	8.000	17
MKH2018	y2018_d60	3300	3	10.000	21
MKH2018	y2018_d7	3223	3	6.000	14

Table S10

Current retrospective scheme levels and their paired contrasts. Intervals condition on trained models.

region	scheme	AUC_95CI	n_pos	n_neg
NC	B0	0.726 (0.706–0.745)	2025	3685
NC	H	0.585 (0.538–0.624)	2025	3685
NC	B1	0.697 (0.661–0.729)	2025	3685
NC	B2	0.774 (0.754–0.795)	2025	3685
NC	B3	0.756 (0.725–0.784)	2025	3685
NC	B0_AEF	0.777 (0.756–0.798)	2025	3685
NC	diagnostic_post	0.830 (0.812–0.848)	2025	3685
Lushan	B0	0.568 (0.514–0.630)	1286	2572
Lushan	H	0.724 (0.666–0.771)	1286	2572
Lushan	B1	0.728 (0.667–0.775)	1286	2572
Lushan	B2	0.594 (0.535–0.654)	1286	2572
Lushan	B3	0.736 (0.675–0.780)	1286	2572
Lushan	B0_AEF	0.600 (0.542–0.659)	1286	2572
Lushan	diagnostic_post	0.713 (0.660–0.764)	1286	2572

region	contrast	effect_95CI
NC	B3-B1	+0.059 (+0.044 to +0.077)
NC	B1-B0	-0.030 (-0.065 to +0.001)
NC	B2-B0	+0.048 (+0.029 to +0.068)
NC	B0_AEF-B0	+0.051 (+0.033 to +0.067)
NC	diagnostic_post-B2	+0.056 (+0.042 to +0.069)
Lushan	B3-B1	+0.008 (-0.007 to +0.022)
Lushan	B1-B0	+0.160 (+0.070 to +0.238)
Lushan	B2-B0	+0.026 (-0.030 to +0.073)
Lushan	B0_AEF-B0	+0.032 (-0.026 to +0.081)
Lushan	diagnostic_post-B2	+0.119 (+0.097 to +0.142)

Table S11

History-operator and training-control sensitivities, followed by near/far support counts for the main designs. Uniform 30 m is the previous operator. The identity operator removes only a training positive's own source, keeping all legitimate historical neighbours at test time. A date-qualified training set does not establish that the inventory version was publicly available in the target year.

design	B0	H	B1	B2	B3	B0_AEF
NC_strict_identity	0.726	0.585	0.697	0.774	0.756	0.777
NC_legacy_identity	0.731	0.597	0.699	0.778	0.751	0.782
NC_legacy_radius30	0.731	0.597	0.699	0.778	0.749	0.782
Lushan_legacy_identity	0.568	0.724	0.728	0.594	0.736	0.600
Lushan_legacy_radius30	0.568	0.714	0.725	0.594	0.733	0.600

design	subset	n_pos	n_neg	estimated
NC_strict_identity	all	2025	3685	True
NC_strict_identity	near_le100m	70	25	False
NC_strict_identity	far_gt100m	1955	3660	True
NC_strict_identity	post_diagnostic_common	2025	3685	True
Lushan_legacy_identity	all	1286	2572	True
Lushan_legacy_identity	near_le100m	608	319	True
Lushan_legacy_identity	far_gt100m	678	2253	True
Lushan_legacy_identity	post_diagnostic_common	1286	2572	True

region	subset	contrast	effect_95CI	n_pos	n_neg
NC	far_gt100m	B3-B1	+0.061 (+0.046 to +0.079)	1955	3660
NC	far_gt100m	B1-B0	-0.032 (-0.067 to +0.000)	1955	3660
NC	far_gt100m	B2-B0	+0.048 (+0.028 to +0.069)	1955	3660
NC	far_gt100m	B0_AEF-B0	+0.051 (+0.033 to +0.069)	1955	3660
Lushan	near_le100m	B3-B1	+0.013 (-0.036 to +0.056)	608	319
Lushan	near_le100m	B1-B0	+0.124 (+0.064 to +0.180)	608	319
Lushan	near_le100m	B2-B0	+0.025 (-0.045 to +0.075)	608	319
Lushan	near_le100m	B0_AEF-B0	+0.037 (-0.034 to +0.090)	608	319
Lushan	far_gt100m	B3-B1	+0.015 (-0.015 to +0.042)	678	2253
Lushan	far_gt100m	B1-B0	+0.033 (-0.046 to +0.118)	678	2253
Lushan	far_gt100m	B2-B0	-0.005 (-0.066 to +0.055)	678	2253
Lushan	far_gt100m	B0_AEF-B0	-0.006 (-0.066 to +0.058)	678	2253

Table S12

Map event-year differences with current binary ROC-AUC and area-capture definitions. Capture changes are fractions (multiply by 100 for percentage points); denominators are the specified evaluated domains.

event	domain	model	cap10	cap10_lo	cap10_hi	auc	auc_lo	auc_hi
RER2023	legacy_target_conditioned	LightGBM	0.158	0.137	0.180	0.050	0.043	0.060
RER2023	legacy_target_conditioned	CNN2D	0.104	0.080	0.127	0.029	0.022	0.036
GDCLD_LUS2022	legacy_target_conditioned	LightGBM	0.257	0.212	0.295	0.103	0.082	0.127
GDCLD_LUS2022	legacy_target_conditioned	CNN2D	0.248	0.191	0.306	0.094	0.073	0.122
GDCLD_MES2019	legacy_target_conditioned	LightGBM	0.033	0.002	0.057	0.005	-0.004	0.014
GDCLD_MES2019	legacy_target_conditioned	CNN2D	0.045	0.014	0.073	0.012	0.002	0.021
GDCLD_PAL2018	legacy_target_conditioned	LightGBM	0.248	0.177	0.311	0.136	0.093	0.176
GDCLD_PAL2018	legacy_target_conditioned	CNN2D	0.295	0.190	0.371	0.142	0.086	0.191
GDCLD_SUM2022	legacy_target_conditioned	LightGBM	0.281	0.196	0.350	0.147	0.104	0.200
GDCLD_SUM2022	legacy_target_conditioned	CNN2D	0.161	0.089	0.233	0.089	0.050	0.127
IBU2018	legacy_target_conditioned	LightGBM	0.387	0.331	0.447	0.299	0.266	0.332
IBU2018	legacy_target_conditioned	CNN2D	0.458	0.341	0.581	0.277	0.230	0.329
JIS2023	legacy_target_conditioned	LightGBM	0.074	0.046	0.102	0.037	0.021	0.053
JIS2023	legacy_target_conditioned	CNN2D	0.052	0.018	0.080	0.013	-0.007	0.033
LUD2022	legacy_target_conditioned	LightGBM	0.315	0.262	0.348	0.131	0.106	0.154
LUD2022	legacy_target_conditioned	CNN2D	0.336	0.274	0.382	0.132	0.112	0.155
MKH2018	legacy_target_conditioned	LightGBM	0.254	0.218	0.286	0.101	0.078	0.122
MKH2018	legacy_target_conditioned	CNN2D	0.247	0.178	0.300	0.105	0.060	0.142
FL2023	administrative_common_support_P2	LightGBM	0.193	0.143	0.254	0.108	0.079	0.141
FL2023	administrative_common_support_P2	CNN2D	0.103	0.051	0.154	0.088	0.059	0.117

Additional sensitivity and representation evidence

Table S13

Training-year × prediction-year decomposition per event (AlphaEarth). AUC $a \rightarrow b$ is the out-of-fold AUC of models trained with year a inputs and applied with year b inputs. Components are relative to the prior-year model (Y-1→Y-1), with 95% cluster-bootstrap CIs.

Event	f	Model	AUC Y-1→Y-1	AUC Y-1→Y	AUC Y→Y-1	AUC Y→Y	Prediction-time component	Training component	Event-year increment
Mesetas (Colombia)	0.02	LightGBM	0.855	0.848	0.834	0.861	-0.007 (-0.017, +0.002)	-0.021 (-0.037, -0.003)	+0.006 (-0.006, +0.019)
	0.02	CNN2D	0.878	0.870	0.865	0.897	-0.007 (-0.022, +0.010)	-0.013 (-0.025, +0.000)	+0.019 (+0.007, +0.032)
Jishishan (China)	0.04	LightGBM	0.591	0.568	0.542	0.617	-0.023 (-0.048, +0.010)	-0.048 (-0.062, -0.034)	+0.026 (+0.004, +0.048)
	0.04	CNN2D	0.734	0.656	0.671	0.717	-0.078 (-0.131, -0.014)	-0.063 (-0.130, -0.008)	-0.017 (-0.056, +0.016)
Nalgae, Mindanao (Philippines)	0.18	LightGBM	0.804	0.801	0.770	0.839	-0.003 (-0.027, +0.018)	-0.034 (-0.061, -0.003)	+0.036 (+0.016, +0.064)
	0.18	CNN2D	0.768	0.754	0.761	0.753	-0.013 (-0.034, +0.007)	-0.006 (-0.029, +0.018)	-0.015 (-0.044, +0.015)
Helene, southern Appalachians (USA)	0.26	LightGBM	0.815	0.849	0.795	0.888	+0.034 (+0.026, +0.043)	-0.020 (-0.031, -0.010)	+0.073 (+0.064, +0.084)
	0.26	CNN2D	0.801	0.799	0.760	0.866	-0.002 (-0.017, +0.010)	-0.041 (-0.064, -0.011)	+0.065 (+0.055, +0.078)
Palu (Indonesia)	0.26	LightGBM	0.720	0.705	0.695	0.835	-0.015 (-0.050, +0.018)	-0.025 (-0.054, +0.007)	+0.115 (+0.081, +0.154)
	0.26	CNN2D	0.737	0.768	0.745	0.867	+0.031 (-0.004, +0.078)	+0.009 (-0.028, +0.046)	+0.131 (+0.085, +0.177)
Mangkhut, Itogon (Philippines)	0.29	LightGBM	0.818	0.832	0.745	0.873	+0.014 (+0.002, +0.026)	-0.073 (-0.103, -0.045)	+0.055 (+0.039, +0.069)
	0.29	CNN2D	0.763	0.835	0.728	0.870	+0.072 (+0.024, +0.119)	-0.035 (-0.089, +0.017)	+0.107 (+0.057, +0.159)
Eastern Iburi (Japan)	0.32	LightGBM	0.829	0.761	0.702	0.926	-0.068 (-0.110, -0.030)	-0.127 (-0.176, -0.076)	+0.098 (+0.075, +0.122)
	0.32	CNN2D	0.830	0.726	0.587	0.948	-0.104 (-0.159, -0.054)	-0.243 (-0.304, -0.175)	+0.118 (+0.078, +0.156)
Luding (China)	0.32	LightGBM	0.757	0.760	0.720	0.842	+0.003 (-0.010, +0.017)	-0.037 (-0.062, -0.008)	+0.085 (+0.066, +0.100)
	0.32	CNN2D	0.796	0.798	0.656	0.903	+0.001 (-0.048, +0.033)	-0.140 (-0.194, -0.067)	+0.107 (+0.085, +0.128)
Chittagong (Bangladesh)	0.38	LightGBM	0.808	0.831	0.768	0.936	+0.023 (+0.015, +0.031)	-0.040 (-0.067, -0.013)	+0.128 (+0.106, +0.148)
	0.38	CNN2D	0.804	0.832	0.737	0.894	+0.028 (+0.015, +0.037)	-0.067 (-0.092, -0.040)	+0.090 (+0.070, +0.110)
Northern Vietnam	0.41	LightGBM	0.678	0.702	0.612	0.820	+0.023 (-0.001, +0.051)	-0.067 (-0.098, -0.032)	+0.141 (+0.108, +0.173)
	0.41	CNN2D	0.721	0.727	0.662	0.807	+0.007 (-0.019, +0.028)	-0.059 (-0.095, -0.027)	+0.086 (+0.045, +0.120)
Fujian (China)	0.43	LightGBM	0.822	0.801	0.789	0.890	-0.020 (-0.040, +0.001)	-0.032 (-0.061, +0.002)	+0.069 (+0.050, +0.094)
	0.43	CNN2D	0.800	0.794	0.761	0.825	-0.006 (-0.030, +0.020)	-0.039 (-0.062, -0.006)	+0.025 (-0.005, +0.053)
Luzon (Philippines)	0.43	LightGBM	0.727	0.750	0.687	0.927	+0.023 (+0.004, +0.041)	-0.040 (-0.056, -0.019)	+0.200 (+0.178, +0.224)
	0.43	CNN2D	0.729	0.740	0.656	0.931	+0.011 (-0.009, +0.031)	-0.073 (-0.100, -0.045)	+0.202 (+0.179, +0.230)
Lushan (China)	0.58	LightGBM	0.833	0.869	0.823	0.924	+0.035 (+0.016, +0.057)	-0.010 (-0.028, +0.006)	+0.091 (+0.071, +0.115)
	0.58	CNN2D	0.842	0.860	0.849	0.921	+0.018 (+0.004, +0.034)	+0.006 (-0.005, +0.017)	+0.079 (+0.056, +0.106)
Agatha (Mexico)	0.59	LightGBM	0.766	0.738	0.667	0.910	-0.028 (-0.045, -0.010)	-0.100 (-0.129, -0.072)	+0.144 (+0.116, +0.172)
	0.59	CNN2D	0.789	0.721	0.676	0.882	-0.068 (-0.104, -0.027)	-0.113 (-0.161, -0.068)	+0.093 (+0.066, +0.119)
Emilia-Romagna (Italy)	0.63	LightGBM	0.908	0.888	0.844	0.933	-0.020 (-0.026, -0.014)	-0.064 (-0.078, -0.053)	+0.025 (+0.019, +0.031)
	0.63	CNN2D	0.935	0.837	0.870	0.951	-0.098 (-0.118, -0.078)	-0.065 (-0.081, -0.052)	+0.015 (+0.011, +0.021)
Freddy (Malawi)	0.81	LightGBM	0.853	0.846	0.838	0.912	-0.007 (-0.018, +0.005)	-0.016 (-0.030, -0.002)	+0.058 (+0.038, +0.079)
	0.81	CNN2D	0.833	0.826	0.810	0.871	-0.008 (-0.020, +0.008)	-0.023 (-0.044, -0.004)	+0.038 (+0.015, +0.064)
Pasaman, West Sumatra (Indonesia)	0.85	LightGBM	0.884	0.936	0.863	0.974	+0.052 (+0.033, +0.072)	-0.021 (-0.043, -0.001)	+0.090 (+0.058, +0.124)
	0.85	CNN2D	0.907	0.932	0.839	0.960	+0.025 (+0.011, +0.043)	-0.068 (-0.123, -0.013)	+0.053 (+0.030, +0.082)
São Paulo coast (Brazil)	0.86	LightGBM	0.791	0.748	0.724	0.957	-0.042 (-0.069, -0.011)	-0.066 (-0.118, -0.005)	+0.167 (+0.113, +0.228)
	0.86	CNN2D	0.798	0.761	0.760	0.885	-0.037 (-0.060, -0.013)	-0.038 (-0.085, +0.020)	+0.088 (+0.045, +0.141)

Table S14

Increments for the year after next (Y+2; 17 events; Helene has no 2026 product). The decay ratio d_2/d_1 is per event; the pooled decay uses events with a visible year-after signal (Text S5).

Event	f	Model	Event year d0	Year after d1	Year after next d2	d2/d1	Year-after signal visible
Mesetas (Colombia)	0.02	CNN2D	+0.020	+0.081	+0.053	0.65	yes
Mesetas (Colombia)	0.02	LightGBM	+0.006	+0.090	+0.062	0.69	yes
Jishishan (China)	0.04	CNN2D	-0.017	+0.040	+0.073	1.84	yes
Jishishan (China)	0.04	LightGBM	+0.026	+0.026	+0.021	0.80	yes
Nalgae, Mindanao (Philippines)	0.18	CNN2D	-0.015	-0.024	-0.007	0.29	no
Nalgae, Mindanao (Philippines)	0.18	LightGBM	+0.036	+0.017	+0.042	2.53	no
Palu (Indonesia)	0.26	CNN2D	+0.131	+0.209	+0.205	0.98	yes
Palu (Indonesia)	0.26	LightGBM	+0.115	+0.256	+0.242	0.95	yes
Mangkhut, Itogon (Philippines)	0.29	CNN2D	+0.107	+0.071	+0.013	0.19	yes
Mangkhut, Itogon (Philippines)	0.29	LightGBM	+0.055	+0.057	+0.001	0.02	yes
Eastern Iburi (Japan)	0.32	CNN2D	+0.118	+0.152	+0.152	1.00	yes
Eastern Iburi (Japan)	0.32	LightGBM	+0.098	+0.152	+0.150	0.99	yes
Luding (China)	0.32	CNN2D	+0.107	+0.134	+0.118	0.88	yes
Luding (China)	0.32	LightGBM	+0.085	+0.139	+0.126	0.91	yes
Chittagong (Bangladesh)	0.38	CNN2D	+0.090	+0.061	+0.022	0.37	yes
Chittagong (Bangladesh)	0.38	LightGBM	+0.128	+0.105	+0.069	0.65	yes
Northern Vietnam	0.41	CNN2D	+0.086	+0.075	+0.021	0.27	yes
Northern Vietnam	0.41	LightGBM	+0.141	+0.145	+0.081	0.56	yes
Fujian (China)	0.43	CNN2D	+0.025	+0.016	+0.013	0.80	no
Fujian (China)	0.43	LightGBM	+0.069	+0.075	+0.046	0.61	yes
Luzon (Philippines)	0.43	CNN2D	+0.202	+0.209	+0.162	0.77	yes
Luzon (Philippines)	0.43	LightGBM	+0.200	+0.219	+0.175	0.80	yes
Lushan (China)	0.58	CNN2D	+0.079	+0.080	+0.064	0.80	yes
Lushan (China)	0.58	LightGBM	+0.091	+0.090	+0.073	0.81	yes
Agatha (Mexico)	0.59	CNN2D	+0.093	+0.054	+0.025	0.47	yes
Agatha (Mexico)	0.59	LightGBM	+0.144	+0.114	+0.070	0.61	yes
Emilia-Romagna (Italy)	0.63	CNN2D	+0.015	+0.017	+0.012	0.71	yes
Emilia-Romagna (Italy)	0.63	LightGBM	+0.025	+0.024	+0.015	0.64	yes
Freddy (Malawi)	0.81	CNN2D	+0.038	+0.028	+0.017	0.60	yes
Freddy (Malawi)	0.81	LightGBM	+0.058	+0.044	+0.024	0.55	yes
Pasaman, West Sumatra (Indonesia)	0.85	CNN2D	+0.053	+0.037	+0.018	0.49	yes
Pasaman, West Sumatra (Indonesia)	0.85	LightGBM	+0.090	+0.076	+0.064	0.84	yes
São Paulo coast (Brazil)	0.86	CNN2D	+0.088	+0.064	+0.045	0.70	yes
São Paulo coast (Brazil)	0.86	LightGBM	+0.167	+0.155	+0.140	0.91	yes

Recovery adjustment of the AEF exposure model. The year-after product covers lags f to f + 1 years. With exponential recovery at rate λ, its signal is proportional to exp(-λf), so the ratio d_0/d_1 contains a factor exp(λf). We estimated λ from the products of the year after next (Y+2, 17 events) as λ = -ln q, with $q = \Sigma d_2/\Sigma d_1$ over events whose year-after increment is distinguishable from zero. The interval for q comes from an event bootstrap with 2,000 resamples. We then refitted the joint model with d_1 multiplied by exp(λf), its variance by exp($2\lambda f$) and the covariance by exp(λf).

Quantity	Point LightGBM	Patch CNN2D
Decay ratio q (event bootstrap 95% CI)	0.770 (0.661–0.854)	0.762 (0.592–0.898)
λ (per year)	0.26	0.27
Unadjusted: slope p; A; f_{50}	0.0005; 1.16; 0.24	0.0003; 1.14; 0.26
Adjusted: slope p; A; f_{50}	0.004; 0.96; 0.23	0.002; 0.99; 0.26
Adjusted with λ at the CI ends: slope p; A	0.002–0.013; 0.87–1.03	0.001–0.011; 0.87–1.08

Table S15

Controlled re-analysis of the setting of Cheng et al. (2026). n.a.: not computed for the reconstructed protocol. **P1:** random 70:30 split; five seeds; t-based CIs. **P2:** spatial 5-fold cross-validation with a 500 m buffer; 30-cluster bootstrap. **P1 paper:** a reconstructed protocol with the documented factor differences. **LCF:** our six terrain factors; the original study used 14.

Protocol	Sample	Model	AUC LCF	AUC AE2022 (pre-event)	AUC AE2023 (event year)	Event year (AE2023 - AE2022)	Placebo (AE2022 - AE2021)	Pre-event vs LCF (AE2022 - LCF)
P1	2,614 + 2,614	CNN1D	0.864	0.918	0.953	+0.034 (+0.027, +0.041)	+0.000 (-0.008, +0.008)	+0.055 (+0.043, +0.067)
P1	2,614 + 2,614	CNN2D	0.895	0.944	0.961	+0.017 (+0.012, +0.022)	-0.001 (-0.009, +0.008)	+0.048 (+0.038, +0.059)
P1	2,614 + 2,614	ViT	0.904	0.947	0.967	+0.020 (+0.012, +0.028)	-0.002 (-0.011, +0.007)	+0.043 (+0.033, +0.053)
P1	2,614 + 2,614	LightGBM	0.860	0.924	0.956	+0.032 (+0.025, +0.038)	+0.000 (-0.003, +0.004)	+0.065 (+0.055, +0.075)
P1	10,365 + 10,365	CNN1D	0.881	0.943	0.970	+0.027 (+0.024, +0.031)	+0.000 (-0.002, +0.002)	+0.061 (+0.056, +0.066)
P1	10,365 + 10,365	CNN2D	0.916	0.969	0.980	+0.011 (+0.008, +0.013)	+0.001 (-0.004, +0.006)	+0.053 (+0.049, +0.057)
P1	10,365 + 10,365	ViT	0.948	0.973	0.986	+0.013 (+0.009, +0.016)	-0.002 (-0.004, +0.001)	+0.025 (+0.021, +0.030)
P1	10,365 + 10,365	LightGBM	0.884	0.942	0.969	+0.027 (+0.024, +0.030)	-0.002 (-0.003, -0.001)	+0.058 (+0.055, +0.061)
P2	2,614 + 2,614	CNN1D	0.792	0.838	0.915	+0.076 (+0.039, +0.117)	-0.006 (-0.018, +0.006)	+0.048 (+0.028, +0.074)
P2	2,614 + 2,614	CNN2D	0.818	0.858	0.902	+0.042 (+0.009, +0.077)	+0.002 (-0.017, +0.021)	+0.040 (+0.015, +0.070)
P2	2,614 + 2,614	ViT	0.809	0.834	0.897	+0.064 (+0.029, +0.107)	-0.010 (-0.028, +0.007)	+0.037 (+0.005, +0.077)
P2	2,614 + 2,614	LightGBM	0.783	0.829	0.913	+0.084 (+0.044, +0.129)	-0.003 (-0.015, +0.009)	+0.046 (+0.015, +0.078)
P2	10,365 + 10,365	CNN1D	0.800	0.857	0.929	+0.069 (+0.035, +0.108)	-0.012 (-0.030, +0.001)	+0.060 (+0.036, +0.089)
P2	10,365 + 10,365	CNN2D	0.830	0.861	0.920	+0.057 (+0.029, +0.089)	+0.003 (-0.010, +0.017)	+0.038 (+0.009, +0.072)
P2	10,365 + 10,365	ViT	0.812	0.851	0.936	+0.086 (+0.046, +0.132)	-0.011 (-0.030, +0.004)	+0.034 (+0.007, +0.063)
P2	10,365 + 10,365	LightGBM	0.808	0.848	0.928	+0.079 (+0.041, +0.121)	-0.009 (-0.022, +0.002)	+0.041 (+0.014, +0.068)
P1paper	2,614 + 2,614	CNN1D	0.868	0.928	0.958	+0.031 (+0.023, +0.038)	n.a.	+0.059 (+0.048, +0.070)
P1paper	2,614 + 2,614	CNN2D	0.910	0.953	0.969	+0.015 (+0.012, +0.019)	n.a.	+0.044 (+0.038, +0.049)
P1paper	2,614 + 2,614	ViT	0.919	0.955	0.972	+0.016 (+0.011, +0.022)	n.a.	+0.037 (+0.031, +0.043)

P1 paper selects batch size and learning rate using the same 30% split on which its AUC is reported. It reproduces that selection procedure and is not an independent test estimate; P1 and P2 use inner validation for early stopping. The principal annual audit uses fixed settings.

Table S16

Cross-year stability of the two embedding products at control points. Stability index = (c_same - c_rand)/(1 - c_rand).

Event (control points)	Years	AlphaEarth cosine, same site	AlphaEarth cosine, random pairs	AlphaEarth stability index	TESSERA cosine, same site	TESSERA cosine, random pairs	TESSERA stability index
Helene, southern Appalachians (USA)	2022→2023	0.982	0.732	0.933	0.914	0.698	0.715
Helene, southern Appalachians (USA)	2023→2024	0.983	0.742	0.935	0.908	0.704	0.689
Emilia-Romagna (Italy)	2021→2022	0.973	0.584	0.936	0.910	0.516	0.814
Jishishan (China)	2021→2022	0.977	0.688	0.925	0.860	0.638	0.613
Lushan (China)	2020→2021	0.979	0.698	0.930	0.873	0.701	0.578
Mesetas (Colombia)	2017→2018	0.965	0.671	0.894	0.840	0.715	0.439
Luding (China)	2020→2021	0.984	0.612	0.958	0.888	0.630	0.698
Fujian (China)	2021→2022	0.950	0.746	0.801	0.851	0.711	0.484

Table S17

Typhoon Mangkhut: event-year and year-after increments after excluding points near mapped mining areas (Maus et al. 2022).

Points kept	Model	Points (landslides)	Event year d0	Year after d1	Ratio d0/d1 (95% range)
all	LightGBM	3,300 (1,100)	+0.055 (+0.039, +0.069)	+0.057 (+0.041, +0.072)	0.97 (0.82–1.12)
all	CNN2D	3,300 (1,100)	+0.107 (+0.057, +0.159)	+0.071 (+0.035, +0.103)	1.52 (1.27–1.86)
> 500 m from mapped mining areas	LightGBM	3,227 (1,058)	+0.056 (+0.036, +0.072)	+0.065 (+0.045, +0.085)	0.85 (0.70–1.00)
> 500 m from mapped mining areas	CNN2D	3,227 (1,058)	+0.092 (+0.047, +0.141)	+0.073 (+0.036, +0.110)	1.26 (1.00–1.58)
> 1000 m from mapped mining areas	LightGBM	3,071 (984)	+0.052 (+0.033, +0.070)	+0.059 (+0.038, +0.079)	0.89 (0.73–1.09)
> 1000 m from mapped mining areas	CNN2D	3,071 (984)	+0.094 (+0.053, +0.138)	+0.064 (+0.028, +0.093)	1.48 (1.20–2.09)

Table S18

Versions of the annual embedding files used. On 16 October 2026 every source file behind the data used was queried with an HTTP HEAD request; all requests returned status 200. Sizes are those of the complete source files, of which only small parts were read. The full lists, with the ETag, size and last-modified date of every file, are Supplementary Data S1 (AlphaEarth) and S2 (TESSERA) in Online Resource 2.

Product	Version and path	Years	Source files	Used for	Last modified (UTC)	Size of the source files
AlphaEarth Satellite Embedding, annual	V1; Source Cooperative `tge-labs/aef/v1/annual`	2017–2025	291 (4,049 blocks read)	all AlphaEarth analyses	2025-11-04 to 2026-03-22	0.84 TB
TESSERA annual representations	v1; Source Cooperative `tessera/tessera/npy/v1`	2017–2025	3,440 (embedding and scale files)	Emilia-Romagna, Fujian, Helene, Jishishan, Luding, Lushan, Mesetas	2026-06-24 to 2026-07-30	232.7 GB
TESSERA annual representations	v1.1-cam; `tessera/tessera/npy/v1.1-cam`	2017–2024	512	Agatha, Freddy, São Paulo; Mesetas (version check)	2026-08-12 to 2026-08-13	40.7 GB

File	SHA-256
AlphaEarth tile index (`aef_index.parquet`, 4 October 2026)	`f738e7d274ad582e56e20a3a8b444c6f2a3ece5781f8f9855bb7ca3d9ed2942f`
TESSERA manifest v1 (`manifest_v1.parquet`, 14 October 2026)	`b7d0717c20f3955b4832ee006aa6d835f18b3a376083f7616205add134246c5a`
TESSERA manifest v1.1-cam (`manifest_v1.1-cam.parquet`, 14 October 2026)	`3fc630a805a04f9789c07b1248aaf9541122944115abc3ffd99363ff3387c99a`
Supplementary Data S1 (AlphaEarth file list)	`5f4b94abb832c1f5673c06544dcebac024265f8b71571ee3aa18c50f1e40779d`
Supplementary Data S2 (TESSERA file list)	`bd8215543029419fb62c3247d8cb27bccc0c7dc4c3d194876a91ec53b95acbb2`

AUC aggregation, preprocessing and support sensitivities

Table S19

Annual AEF increments under pooled out-of-fold and within-fold pair-weighted AUC. Event rows are full-sample point estimates; within-fold intervals are paired spatial-cluster intervals. The primary bootstrap-mean event summaries remain in Table S2. No score calibration or spatial redesign is introduced.

Event	Point pooled	Point within-fold (95% CI)	Patch pooled	Patch within-fold (95% CI)
Chittagong	+0.1281	+0.108 (+0.090, +0.127)	+0.0903	+0.079 (+0.059, +0.100)
São Paulo	+0.1666	+0.166 (+0.104, +0.245)	+0.0876	+0.077 (+0.038, +0.132)
Fujian	+0.0687	+0.061 (+0.036, +0.095)	+0.0249	+0.026 (-0.004, +0.056)
Agatha	+0.1441	+0.132 (+0.106, +0.160)	+0.0927	+0.089 (+0.064, +0.115)
Freddy	+0.0583	+0.072 (+0.042, +0.098)	+0.0384	+0.059 (+0.035, +0.085)
Nalgae (Mindanao)	+0.0355	+0.021 (-0.003, +0.055)	-0.0146	-0.003 (-0.023, +0.011)
Luzon	+0.1996	+0.189 (+0.166, +0.217)	+0.2019	+0.190 (+0.166, +0.222)
Northern Vietnam	+0.1414	+0.133 (+0.099, +0.173)	+0.0862	+0.084 (+0.041, +0.122)
Lushan	+0.0912	+0.121 (+0.096, +0.153)	+0.0785	+0.123 (+0.088, +0.165)
Mesetas	+0.0061	+0.015 (+0.005, +0.026)	+0.0199	+0.017 (+0.003, +0.032)
Palu	+0.1149	+0.108 (+0.078, +0.148)	+0.1306	+0.124 (+0.079, +0.174)
Pasaman	+0.0896	+0.094 (+0.066, +0.134)	+0.0533	+0.057 (+0.034, +0.088)
Helene	+0.0733	+0.070 (+0.059, +0.082)	+0.0649	+0.058 (+0.049, +0.073)
Eastern Iburi	+0.0980	+0.095 (+0.074, +0.123)	+0.1178	+0.103 (+0.076, +0.133)
Jishishan	+0.0259	-0.010 (-0.028, +0.011)	-0.0173	-0.008 (-0.038, +0.026)
Luding	+0.0849	+0.044 (+0.037, +0.058)	+0.1072	+0.065 (+0.048, +0.090)
Mangkhut	+0.0551	+0.055 (+0.040, +0.074)	+0.1073	+0.083 (+0.045, +0.128)
Emilia-Romagna	+0.0248	+0.037 (+0.029, +0.047)	+0.0155	+0.031 (+0.026, +0.039)

The arithmetic event average and random-effects summary are different quantities. The latter uses each event's bootstrap mean and standard error, as in the retained principal estimator.

Model	AUC aggregation	Event arithmetic mean	Random-effects mean (95% CI)	Positive events
CNN2D	pooled	0.0714	+0.070 (+0.048, +0.093)	16/18
CNN2D	within	0.0697	+0.069 (+0.050, +0.088)	16/18
LightGBM	pooled	0.0892	+0.087 (+0.065, +0.110)	18/18
LightGBM	within	0.0840	+0.082 (+0.062, +0.103)	17/18

Table S20

Optical seasonal comparison under both AUC aggregations. The absolute levels average ten separately evaluated three-date draws; all confidence intervals use paired spatial and draw resampling. The common supports contain 281/972 positives/controls at Iburi and 315/442 at Mangkhut.

Event	Year / cutoff (days)	Pooled AUC (95% CI)	Within-fold AUC (95% CI)
Eastern Iburi	2017 / -1	0.429 (0.381, 0.485)	0.533 (0.493, 0.577)
Eastern Iburi	2017 / 60	0.397 (0.355, 0.450)	0.490 (0.450, 0.528)
Eastern Iburi	2018 / -1	0.420 (0.373, 0.480)	0.551 (0.510, 0.588)
Eastern Iburi	2018 / 60	0.811 (0.762, 0.847)	0.844 (0.768, 0.881)
Mangkhut	2017 / -1	0.516 (0.469, 0.554)	0.549 (0.493, 0.603)
Mangkhut	2017 / 60	0.596 (0.549, 0.635)	0.616 (0.570, 0.670)
Mangkhut	2018 / -1	0.475 (0.437, 0.515)	0.525 (0.486, 0.566)
Mangkhut	2018 / 60	0.786 (0.755, 0.814)	0.783 (0.746, 0.824)

Seasonal excess: [2018 (+60 minus -1 day)] minus [2017 (+60 minus -1 day)].

Event	Pooled (95% CI)	Within-fold (95% CI)	Equal-fold point estimate
Eastern Iburi	+0.423 (+0.353, +0.479)	+0.335 (+0.255, +0.402)	0.283
Mangkhut	+0.231 (+0.164, +0.293)	+0.191 (+0.117, +0.260)	0.169

Event	Positive counts in folds 0–4	Control counts in folds 0–4
Eastern Iburi	46, 102, 120, 9, 4	295, 122, 158, 205, 192
Mangkhut	34, 133, 97, 2, 49	143, 101, 99, 72, 27

Small positive folds contribute few sample pairs to the pair-weighted statistic. Its difference from pooled AUC reflects the excluded cross-fold pairs and potentially different model score scales; it is not attributed solely to calibration. The lower pooled pre-event Iburi level therefore does not establish absence of pre-event information.

Table S21

AEF patch missingness and the targeted imputation sensitivity. The first table summarizes all 69 primary event-year arrays across 18 events after original eligibility. The maximum is taken across an event's available primary years; the accompanying CSV gives every event-year, before and after eligibility, plus class/fold counts. A spatial cell is missing if any of its 64 channels is NaN; a patch is affected if any cell is missing. No infinite values were found.

Event	Primary years scanned	Max missing values (%)	Max missing cells (%)	Max affected patches (%)
Chittagong	2021, 2022, 2023, 2024	0.3338	0.3338	1.302
São Paulo	2021, 2022, 2023, 2024	0.0380	0.0380	0.139
Fujian	2021, 2022, 2023, 2024	0.0000	0.0000	0.000
Agatha	2020, 2021, 2022, 2023	0.0000	0.0000	0.000
Freddy	2021, 2022, 2023, 2024	0.0595	0.0595	0.218
Nalgae (Mindanao)	2020, 2021, 2022, 2023	0.0000	0.0000	0.000
Luzon	2021, 2022, 2023, 2024	0.1094	0.1094	0.387
Northern Vietnam	2021, 2022, 2023, 2024	0.0221	0.0221	0.101
Lushan	2020, 2021, 2022, 2023	0.1602	0.1602	0.648
Mesetas	2017, 2018, 2019, 2020	0.1766	0.1766	0.704
Palu	2017, 2018, 2019	0.0338	0.0338	0.307
Pasaman	2020, 2021, 2022, 2023	0.0000	0.0000	0.000
Helene	2022, 2023, 2024, 2025	0.0849	0.0849	0.377
Eastern Iburi	2017, 2018, 2019	0.3006	0.3006	1.203
Jishishan	2021, 2022, 2023, 2024	0.0522	0.0522	0.205
Luding	2020, 2021, 2022, 2023	0.1746	0.1746	0.680
Mangkhut	2017, 2018, 2019	0.3554	0.3554	1.212
Emilia-Romagna	2021, 2022, 2023, 2024	0.1232	0.1232	0.507

Mangkhut was selected by maximum retained missing-cell fraction before refitting. Both 2017 and 2018 have 1,419/399,300 missing cells (0.3554%), affecting 40/3,300 patches (1.212%). Thirty fold/year/seed jobs each fit the two operators, for 60 fits in total; all settings except imputation are paired.

Operator / comparison	Annual AUC increment (95% CI)
Archived prediction	+0.107 (+0.056, +0.157)
Re-fit: global channel mean	+0.107 (+0.056, +0.157)
Re-fit: inner fitting mean	+0.110 (+0.058, +0.160)
Change in annual increment	+0.0024 (+0.0003, +0.0045)

The paired change is +0.00237 (0.00030, 0.00452). It remains below the locally specified 0.01 trigger for considering more events; no additional CNN events were retrained. This check quantifies one deliberately selected high-missingness case. Intervals condition on these refits. The archive contains both raw Mangkhut patch arrays, inner training/validation indices, channel means, per-seed scores and the exact training implementation.

Table S22

Composition of the four-endpoint seasonal common support. Retention fractions use the same initial candidate set within each event and class. GLO-30 local slope is a descriptive summary; its valid counts are supplied in the CSV. All candidates have known WorldCover 2021 v200 classes. "Tree cover" is WorldCover class 10; the complete class distribution is supplied as counts and proportions, including zero-count classes. The 2021 description is later than the 2018 events and does not represent pre-event cover.

Event	Class	Retained / candidate	Slope retained / excluded (°)	Tree cover retained / excluded (%)
Eastern Iburi	Landslide	281/1100 (25.5%)	18.7 / 22.3	66.2 / 71.3
Eastern Iburi	Control	972/2200 (44.2%)	12.5 / 17.6	90.3 / 93.4
Mangkhut	Landslide	315/1100 (28.6%)	31.6 / 31.7	74.6 / 51.8
Mangkhut	Control	442/2200 (20.1%)	23.4 / 28.0	85.7 / 76.5

Table S23

Event-year AEF increments by inventory form. DL: DerSimonian–Laird mean with 95% CI (primary estimator); REML (HKSJ): robustness analysis; drift-corrected: DL mean of d0 - placebo over the events with a Y-2 layer. Trigger groups are shown to expose the confounding with inventory form, not as a separate test. Differences are point inventories minus mapped extents.

Model	Group	k	DL mean (95% CI)	REML (HKSJ 95% CI)	Positive events	Range	Drift-corrected DL (95% CI), k
Point model	Mapped extents (polygons + rasters)	9	+0.0638 (+0.0403, +0.0872)	+0.0641 (+0.0342, +0.0939)	9/9	0.0070 to 0.1161	+0.0472 (+0.0124, +0.0820), 6
Point model	Manual polygons	5	+0.0569 (+0.0276, +0.0861)	+0.0569 (+0.0154, +0.0983)	5/5	0.0248 to 0.0987	+0.0444 (-0.0050, +0.0939), 3
Point model	Labelled rasters (GDCLD)	4	+0.0751 (+0.0169, +0.1333)	+0.0745 (-0.0026, +0.1516)	4/4	0.0070 to 0.1161	+0.0512 (-0.0238, +0.1262), 3
Point model	Point inventories	9	+0.1111 (+0.0771, +0.1451)	+0.1113 (+0.0687, +0.1539)	9/9	0.0368 to 0.2000	+0.1107 (+0.0762, +0.1453), 9
Point model	Earthquake events	7	+0.0721 (+0.0372, +0.1071)	+0.0718 (+0.0339, +0.1098)	7/7	0.0070 to 0.1161	+0.0527 (+0.0012, +0.1041), 5
Point model	Rainfall events	11	+0.0975 (+0.0661, +0.1288)	+0.0978 (+0.0589, +0.1367)	11/11	0.0248 to 0.2000	+0.1017 (+0.0661, +0.1372), 10
Point model	All events	18	+0.0874 (+0.0649, +0.1098)	+0.0876 (+0.0617, +0.1135)	18/18	0.0070 to 0.2000	+0.0848 (+0.0569, +0.1128), 15
Point model	Difference, separate between-event variances	18	+0.0473 (+0.0060, +0.0886)	n.a.	n.a.	n.a.	n.a.
Point model	Difference, REML meta-regression (Knapp–Hartung)	18	+0.0462 (-0.0015, +0.0939)	n.a.	n.a.	n.a.	n.a.
Patch model	Mapped extents (polygons + rasters)	9	+0.0652 (+0.0370, +0.0933)	+0.0660 (+0.0261, +0.1060)	8/9	-0.0169 to 0.1317	+0.0487 (+0.0144, +0.0831), 6
Patch model	Manual polygons	5	+0.0643 (+0.0107, +0.1179)	+0.0643 (-0.0123, +0.1410)	4/5	-0.0169 to 0.1177	+0.0481 (-0.0222, +0.1184), 3
Patch model	Labelled rasters (GDCLD)	4	+0.0677 (+0.0254, +0.1101)	+0.0680 (-0.0053, +0.1414)	4/4	0.0199 to 0.1317	+0.0497 (+0.0058, +0.0935), 3
Patch model	Point inventories	9	+0.0750 (+0.0394, +0.1106)	+0.0750 (+0.0287, +0.1213)	8/9	-0.0131 to 0.2029	+0.0736 (+0.0341, +0.1131), 9
Patch model	Earthquake events	7	+0.0691 (+0.0319, +0.1062)	+0.0692 (+0.0195, +0.1188)	6/7	-0.0169 to 0.1317	+0.0572 (+0.0158, +0.0985), 5
Patch model	Rainfall events	11	+0.0716 (+0.0394, +0.1037)	+0.0717 (+0.0327, +0.1107)	10/11	-0.0131 to 0.2029	+0.0669 (+0.0276, +0.1062), 10
Patch model	All events	18	+0.0705 (+0.0475, +0.0934)	+0.0707 (+0.0434, +0.0979)	16/18	-0.0169 to 0.2029	+0.0637 (+0.0345, +0.0928), 15

Model	Group	k	DL mean (95% CI)	REML (HKSJ 95% CI)	Positive events	Range	Drift-corrected DL (95% CI), k
Patch model	Difference, separate between-event variances	18	+0.0099 (-0.0355, +0.0552)	n.a.	n.a.	n.a.	n.a.
Patch model	Difference, REML meta-regression (Knapp–Hartung)	18	+0.0087 (-0.0476, +0.0650)	n.a.	n.a.	n.a.	n.a.

n.a.: not applicable to a difference between groups. Event-level values are listed in Table S2 and in `inventory_strata_events.csv` of Online Resource 3.

Table S24

Overlap and replacement of the highest-scoring area over Brisighella and Modigliana (329,953 cells at 30 m; mapped landslide prevalence 3.04%). J: weighted Jaccard index; R: share of the earlier year's selected area that is not selected in the later year. The event-year pair is 2022 versus 2023; the pre-event reference is 2021 versus 2022. Landslide share: mapped landslide area as a percentage of the area in each class. Independent random rankings give J = 0.026, 0.053 and 0.111 and R = 0.95, 0.90 and 0.80 at the 5%, 10% and 20% budgets.

Model	Budget	Years compared	J	R	Landslide share: kept / replaced / added (%)	Landslide area in added / replaced cells (% of total)
Point model	5%	2022 vs 2023	0.285	0.557	18.5 / 4.0 / 19.2	17.6 / 3.7
Point model	5%	2021 vs 2022	0.490	0.342	11.5 / 8.8 / 8.4	4.7 / 5.0
Point model	10%	2022 vs 2023	0.366	0.464	15.0 / 2.3 / 15.0	22.8 / 3.5
Point model	10%	2021 vs 2022	0.566	0.277	10.1 / 7.3 / 6.5	5.9 / 6.6
Point model	20%	2022 vs 2023	0.461	0.369	11.1 / 0.9 / 10.0	24.2 / 2.2
Point model	20%	2021 vs 2022	0.650	0.212	8.2 / 5.6 / 4.1	5.7 / 7.8
Patch model	5%	2022 vs 2023	0.353	0.479	16.2 / 7.4 / 13.9	11.0 / 5.8
Patch model	5%	2021 vs 2022	0.513	0.322	13.6 / 10.0 / 8.5	4.5 / 5.3
Patch model	10%	2022 vs 2023	0.402	0.427	13.1 / 4.0 / 11.3	15.9 / 5.6
Patch model	10%	2021 vs 2022	0.548	0.292	10.5 / 7.9 / 6.1	5.9 / 7.6
Patch model	20%	2022 vs 2023	0.471	0.360	10.1 / 1.8 / 8.8	20.8 / 4.4
Patch model	20%	2021 vs 2022	0.599	0.251	7.9 / 5.7 / 4.7	7.7 / 9.4

Spatial-cluster bootstrap intervals at the 10% budget (1,000 replicates; selection recomputed in each replicate) and the range over the five individual spatial designs:

Model	J, 2022 vs 2023 (95% CI)	R, 2022 vs 2023 (95% CI)	J, 2021 vs 2022 (95% CI)	R, 2021 vs 2022 (95% CI)	J difference, reference - event year (95% CI)	Single designs: J event year; J reference
Point model	0.366 (0.323, 0.418)	0.464 (0.410, 0.512)	0.566 (0.539, 0.594)	0.277 (0.254, 0.299)	0.200 (0.159, 0.238)	0.355–0.357; 0.525–0.537
Patch model	0.402 (0.346, 0.453)	0.427 (0.376, 0.486)	0.548 (0.479, 0.603)	0.292 (0.248, 0.352)	0.147 (0.084, 0.195)	0.317–0.394; 0.412–0.494

Intervals condition on the fitted maps. The decomposition is exact: for the point model, 22.8% - 3.5% of the mapped landslide area equals the 19.3-percentage-point capture gain at the 10% budget.

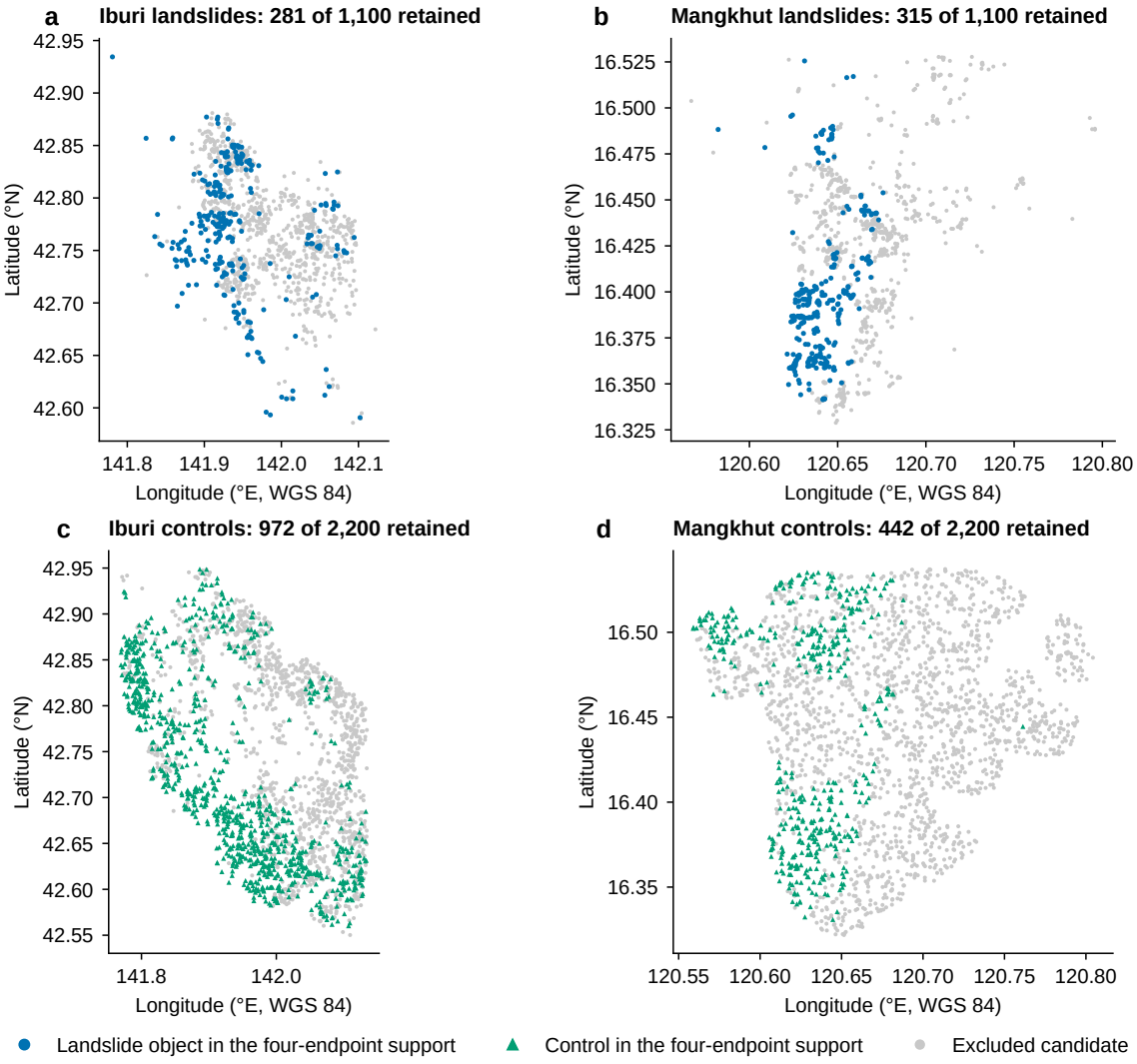


Fig. S1 Optical support selection. Landslide points represent unique inventory objects; controls are shown in separate panels. Coloured symbols mark candidates retained in the principal four-endpoint seasonal comparison (blue circles, landslide objects; green triangles, controls); grey dots mark excluded candidates. The full flow, intersections and selection-variable distributions accompany the archive.

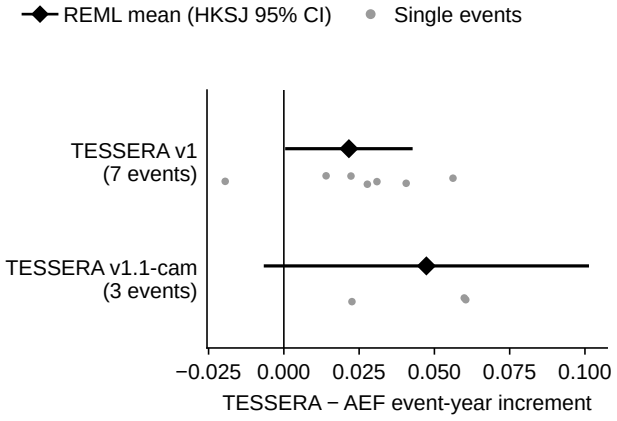


Fig. S2 TESSERA versions. Paired TESSERA-minus-AEF event-year increments within each TESSERA version subset: REML means with HKSJ 95% intervals (diamonds) and single events (dots). In the seven-event v1 subset the excess over AEF was 0.022 (HKSJ interval about 0.000–0.043); the three v1.1-cam events are shown separately because their small number limits version inference. The two version groups comprise different events.

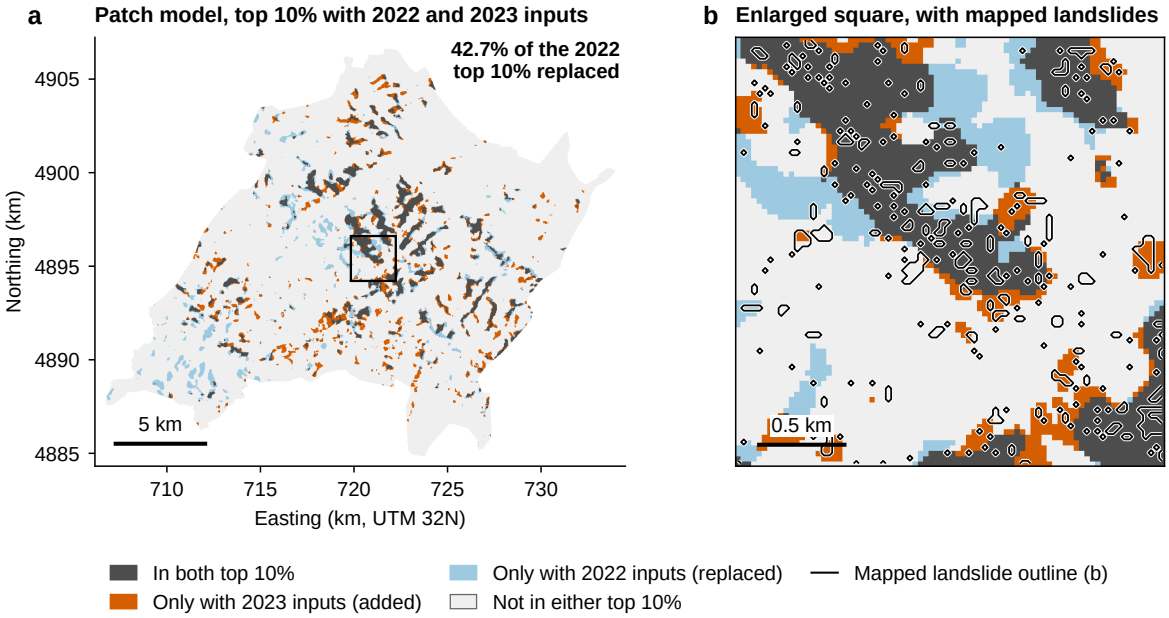


Fig. S3 Patch-model top-area overlap. Patch-model top 10% with prior-year (2022) and event-year (2023) inputs over Brisighella and Modigliana (WGS 84 / UTM zone 32N). (a) Cells selected in both years, only with 2022 inputs (replaced) and only with 2023 inputs (added). (b) The 2.4 km square outlined in (a), centred on the domain's median row and column, with mapped landslide outlines. Scores average five spatial out-of-fold designs.

References

Bartos M et al (2024) mdbartos/pysheds, version 0.5 [software]. Zenodo. https://doi.org/10.5281/zenodo.3822494

Belair GM, Jones ES, Luna LV, Mirus BB (2025) Landslide inventories across the United States (ver. 3.0, February 2025) [dataset]. U.S. Geological Survey data release. https://doi.org/10.5066/P14AJF8I

Cheng Y, Zhu Q, Fan L (2026) From landslide conditioning factors to satellite embeddings: evaluating the utilisation of Google AlphaEarth for landslide susceptibility mapping using deep learning. arXiv:2601.07268 (v2). https://doi.org/10.48550/arXiv.2601.07268

Daly C, Halbleib M, Smith JI et al (2008) Physiographically sensitive mapping of climatological temperature and precipitation across the conterminous United States. Int J Climatol 28:2031–2064. https://doi.org/10.1002/joc.1688

European Space Agency (2022) Copernicus DEM (GLO-30) [dataset]. https://doi.org/10.5270/ESA-c5d3d65

Fang J, Luo W, Huang Q, Li W, Chen Y-C, Liu C-C (2026) Annual geospatial foundation model embeddings for landslide susceptibility assessment in Taiwan. npj Nat Hazards (in press, published online 16 September 2026). https://doi.org/10.1038/s44304-026-00268-7

Li M, Li W, Liu H, Liang C (2026) Leveraging geospatial foundation model embeddings for local-scale landslide susceptibility mapping via positive-unlabeled learning. Research Square. https://doi.org/10.21203/rs.3.rs-10786241/v1

Maus V, Giljum S, da Silva DM et al (2022) An update on global mining land use. Sci Data 9:433. https://doi.org/10.1038/s41597-022-01547-4 (dataset: https://doi.org/10.1594/PANGAEA.942325)

Xu C, Xu X, Shyu JBH (2015) Database and spatial distribution of landslides triggered by the Lushan, China Mw 6.6 earthquake of 20 April 2013. Geomorphology 248:77–92. https://doi.org/10.1016/j.geomorph.2015.07.002 (inventory: https://doi.org/10.5066/F7KS6Q2P)

Zanaga D, Van De Kerchove R, Daems D et al (2022) ESA WorldCover 10 m 2021 v200 [dataset]. Zenodo. https://doi.org/10.5281/zenodo.7254221

Zhuang Y, Hobeichi S, Shi P, Huang F (2026) Evaluating AlphaEarth Foundations embeddings for wildfire susceptibility mapping. arXiv:2608.12663. https://doi.org/10.48550/arXiv.2608.12663